Magneto-optical methods for investigating spin properties of a GaAs spin transport channel

Claassen, P.W.J.C.

Award date:
2007

Magneto-Optical Methods for Investigating Spin Properties of a GaAs Spin Transport Channel

Paul Claassen
November 2007

Report of a master graduation project (September 2006 - November 2007) carried out at the Eindhoven University of Technology in the group Physics of Nanostructures (FNA).

Supervisors: Ir. J.H.H. Rietjens
Prof. dr. B. Koopmans

Abstract

Engineering new semiconductor based electronic devices using the spin degree of freedom in their functionality requires dedicated techniques to determine functionality of individual components. Optical pump-probe techniques having a temporal resolution of up to 100 fs are useful to investigate dynamics related to the electron spin.

Time-resolved Magnetization Modulation Spectroscopy has been used to determine the electron spin relaxation time in an *n*-doped GaAs spin transport channel of a lateral all-electrical spin injection and detection device. The electron spin relaxation time at a temperature of 5 K is found to lie between 0.5 and 3.0 ns, which is short compared to literature values for bulk *n*-GaAs of up to 125 ns. The spatial profile of a spin package under influence of an electric field is monitored, thereby obtaining spin diffusion and spin mobility of respectively 45 ± 10 cm^2s^{-1} and $(1.1 \pm 0.3)\cdot 10^3$ $cm^2V^{-1}s^{-1}$. The influence of carrier recombination on perceived diffusion is shown to obscure measurements when holes are still present.

The optical response of a spin polarised heterostructure is investigated as a function of wavelength. A model has been set up to predict rotation and ellipticity of the magneto-optic Kerr effect in which the optical response of the heterostructure is coupled to a simulated complex linear relational function of z and a depth-dependent complex magneto-optical constant. Measurements of the wavelength dependent optical response show correlation with the calculated effect.

Optical detection of electrical spin injection in the spin transport layer using an AlO_x tunnel barrier and a CoFe ferromagnetic electrode has been attempted. Calculations show that the expected signal is significantly smaller than in comparable results in recent literature.

Contents

1 Introduction

Since the start of the computer era over half a century ago, a continuous race has been going on for faster, smaller and cheaper electronics. A very clear illustration of the development of electronics is Moore's Law[1], a very famous exponential trend that is obeyed to since 1965, stating that the number of transistors on an integrated circuit is doubled every two years. Until now, computer processors perform calculations in their transistors only using the charge of electrons as a source of information.

With the miniaturisation of the elements in an integrated circuit, another attribute of electrons has come forward. Its spin can be used to keep and manipulate information in electronics. The research field of spintronics focuses on actively using this attribute. The first real spintronic effect is the Giant Magnetoresistance (GMR), invented by Albert Fert and Peter Grünberg in 1988[2]. For this effect the 2007 Nobel Prize of Physics has been awarded.

The GMR effect is the enhanced magnetoresistance (MR) of a spintronic device. MR is the change of the resistance due to the presence of a magnetic field. A spin-valve (see figure **1.1**a) is a GMR device that has replaced the read heads of hard disk drives at the beginning of the 1990's. The improved sensitivity to the magnetic field of the bits was an important factor in scaling up the bit density of the drives. Another recent spintronic application is MRAM shown in figure **1.1**b, a non-volatile Magnetic Random Access Memory.

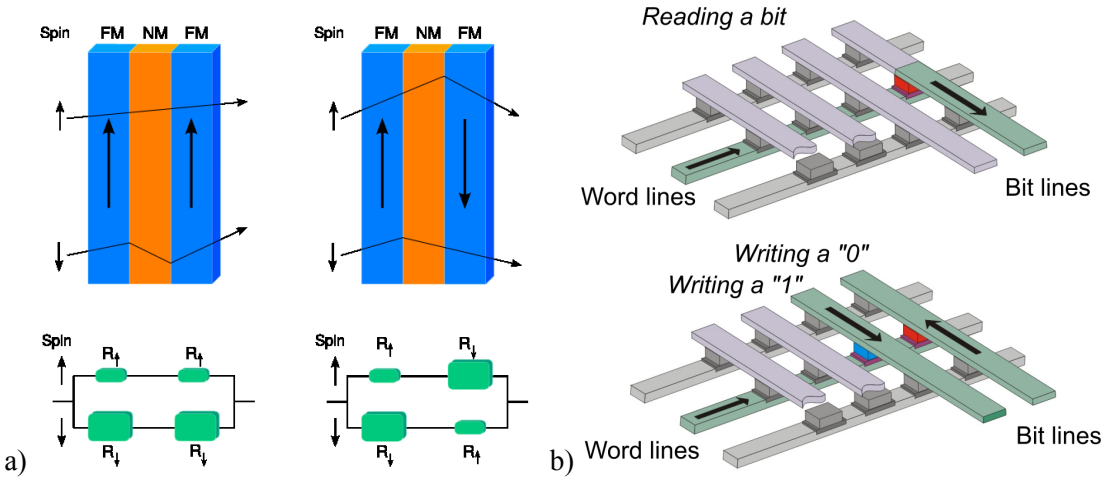

Figure 1.1: Schematic representation of a spin valve (a) and MRAM (b). In the spin valve, the combined resistance of the spin up and spin down channel is dependant on the relative magnetisation of two ferromagnetic layers (FM) separated by a non-magnetic layer (NM). The MRAM device stores bits in a ferromagnetic layer between word and bit lines. For reading, the resistance between two of these lines determines the bit, while for writing the added magnetic fields caused by current in the word and bit lines can switch the layer.

1.1 Spintronics in semiconductors

Compared to non-magnetic metals, the lifetime of spin polarisation in a semiconductor material is orders of magnitude longer[3]. This means that once the electron density in a semiconductor exhibits an imbalance in spin up and spin down, the balance is only slowly recovered. Research has revealed spin lifetimes exceeding 100 nanoseconds in gallium arsenide (GaAs) with specific doping and temperature. While this seems short, the electrons can travel over tens of micrometers, which is a long distance for contemporary electronics. This makes semiconductors ideal for transporting spin polarised electrons over longer distances. Lately, a spin valve has been made using silicon as a transport layer[4]. This is an ideal step towards integrating new spintronic devices in contemporary silicon electronics.

One promising application using a semiconductor as a spin transport channel is the spin transistor, for which a proposal is shown in figure **1.2**[5]. Two ferromagnetic electrodes are grown laterally on top of the semiconductor surface. Each electrode is capable of injecting or collecting a spin polarised current. In between the electrodes, the spin direction can be manipulated by an electric field, using spin-orbit coupling.

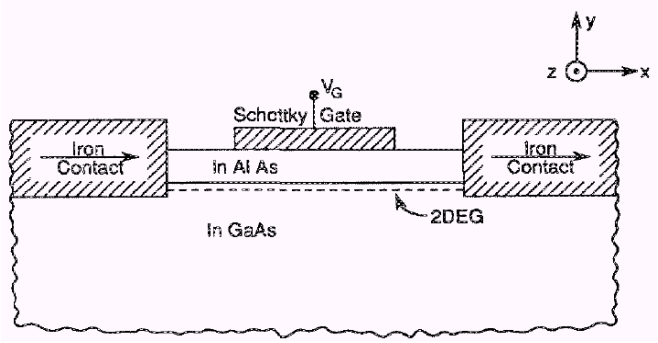

Figure 1.2: Schematic cross section of a proposal for the design of a spin transistor.

1.2 All-electrical spin injection and detection device

In the near past, several designs have been reported for a lateral all-electrical spin injection and detection device[6][7]. In this thesis, a device designed by IMEC Leuven is subject of investigation. Schematically, this device is depicted in figure **1.3**. It consists of a thin layer *n*-doped GaAs, on which two magnetic electrodes are grown, separated by a tunnel barrier. Electrons flowing from one electrode to the channel get spin polarised in the ferromagnetic layer. The resistance of the device depends on the direction of magnetisation of the detection electrode relative to the electron spin and thus to the injection electrode. When the injection magnetisation is switched with an externally applied magnetic field, the detection electrode remains fixed because of its higher coercivity and the device shows MR behaviour.

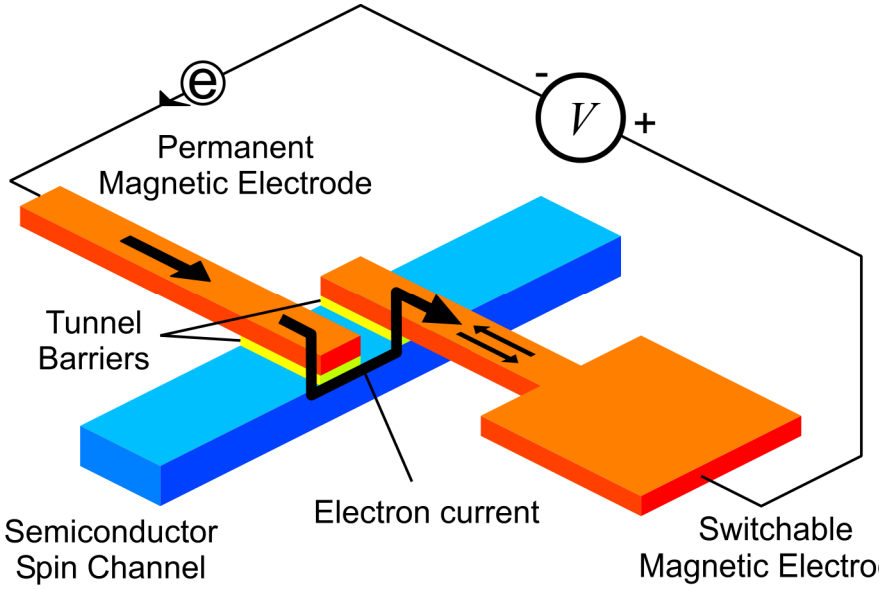

Figure 1.3: Schematic design of all-electrical spin injection and detection device. Spin polarised electrons are injected into the semiconductor spin channel via a switchable magnetic electrode separated by a tunnel barrier. In the same way it is detected by a permanent magnetic electrode.

1.3 This thesis

In this thesis, optical methods are employed with which the all-electrical spin injection and detection device is investigated. The thesis will start with a general description of optical spin injection and detection. Then the design of the device will be explained and a band diagram simulation is carried out. Next, Time-resolved Magnetization Modulation Spectroscopy is described and used to measure the spin lifetime of the device. In the section that follows, a more thoroughly investigation of the source of optical spin detection is performed and a model is created to simulate the optical response. Subsequently, spin transport mechanisms in the device are visualised. The thesis finishes with an attempt of optical detection of electrically injected spins.

2 Optical spin injection and detection

An important part of this thesis consists of descriptions of optical techniques and optical simulations that are used to retrieve information from the all-electrical spin injection and detection device. To understand these techniques, this chapter focuses on some relevant general theoretical aspects. First, an introduction is given on spin polarised electrons in a semiconductor. Then, optical injection is explained, incorporating all steps that follow each other subsequently. The next chapter describes some transport mechanisms which spin is subject to. Finally, optical detection using the magneto-optic Kerr effect is described for a homogeneous sample as well as an arbitrary heterostructure.

2.1 Spin polarised electrons in semiconductors

Spintronics is based upon the quantum mechanical spin of electrons. Electron spin has a fixed magnitude ½$\hbar$, with $\hbar$ Planck's constant divided by 2π. The spin can be oriented in any direction, but quantum mechanics demand that only one of the three dimensions can be defined. The direction of this dimension is chosen in reference to a magnetic field that is relevant for the situation. The spin has either spin up or spin down, corresponding to parallel or antiparallel to the magnetic field.

In magnetised materials, there is an imbalance in electrons with spin up and spin down. The material is said to be spin-polarised. These spin polarised electrons can only exist in electronic bands that are not completely filled, because the Fermi principle states that two electrons cannot have exactly the same state. Full electron bands must thus divide the spin up and spin down electrons equally, resulting in no net spin polarisation. The spin polarisation P_s for a specific selection of electrons, for example a partly filled electronic band, is defined as

$$P_s = \frac{n_\uparrow - n_\downarrow}{n_\uparrow + n_\downarrow} \tag{2.1}$$

where $n_{\uparrow(\downarrow)}$ is the density of the electrons with spin up (down). Spin density is then simply defined as $n_\uparrow - n_\downarrow$. In ferromagnetic materials, spin polarisation exists as a equilibrium state, while in other materials a magnetic field is needed to make spin polarisation energetically favourable. When in the absence of a magnetic field spin polarisation is created in a non-magnetic material, the balance between spin up and spin down electrons will be regained over a period of time, called the spin relaxation time or spin lifetime τ_s.

For semiconductors, spin polarisation can exist for electrons in the valance and the conduction band. In the valance band, it is customary to speak about spin polarised holes, a hole with spin up being a missing electron with spin down. Compared to non-magnetic metals, the spin lifetime of elec-

trons in the conduction band of a semiconductor is very large. It can exceed 100 ns[3] in *n*-doped GaAs at a temperature of 5 K, while the relaxation time for holes is much shorter, usually less than a picosecond[8].

In this thesis, the focus will be on GaAs as a semiconductor. GaAs has a zinc-blende (ZnS) crystal structure, for which the band structure, partly shown in figure **2.1**, is well known[9]. It has a direct band gap at $k = 0$, the so-called Γ-point. Conduction and valance energy bands have a parabolic form near the Γ-point and the curvature defines the effective mass of electrons and holes[10]. In the valance band three types of holes can be distinguished: heavy holes, light holes and split-off holes, each with different quantum numbers for L, S and m_j as summarised in table **2.1**. The angular momentum quantum number m_j determines the spin. For conduction electrons, $m_j = +(-)½$ corresponds to spin up (down). For holes, it is not totally correct to speak about spin, because one has to look at the total angular momentum. In this thesis, a positive (negative) m_j for holes will be referred to as spin up (down).

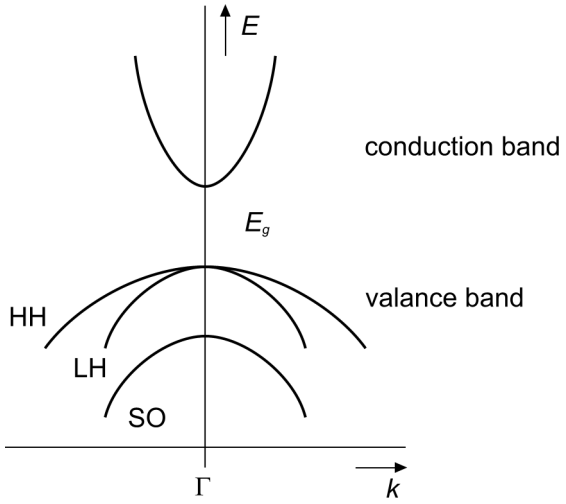

Figure 2.1: Band structure of zinc-blende semiconductor near the Γ-point with heavy hole (HH), light hole (LH) and split-off (SO) band. The band gap has size E_g.

Table 2.1: Quantum numbers for carriers in zinc-blende semiconductor.

carrier	L	*S*	*J*	m_j
conduction electron	0	1/2	1/2	±1/2
heavy hole	1	1/2	3/2	±3/2
light hole	1	1/2	3/2	±1/2
split-off hole	1	1/2	1/2	±1/2

2.2 Optical spin injection

Optical spin injection is a technique to create electron spin polarisation in a semiconductor using circularly polarised light. In this section, the absorption of a short 100 fs circularly polarised laser pulse will be described for *n*-doped GaAs at low temperature, including the processes that take place until the semiconductor has regained equilibrium. In chronological order, these processes are absorption,

hole spin relaxation, electron-hole recombination and electron spin relaxation. They are shown in figure **2.2**, where the density of states as a function of energy $N(E)$, separated for spin up and spin down electrons, is used to visualise the processes. Near the band gap, the exact form of the density of states is defined by the effective mass of electrons or holes. For conduction electrons, the total density of states can be calculated as[10]

$$N(E) = \frac{1}{2\pi^2}\left(\frac{2m_e}{\hbar^2}\right)^{\frac{3}{2}}\left(E - E_c\right)^{\frac{1}{2}} \tag{2.2}$$

where m_e is the effective mass of the electrons and E_c is the energy at the bottom of the conduction band. Although in reality the available states will be filled using a Fermi-Dirac distribution, for the sake of simplicity the states are filled using a step function in figure **2.2**.

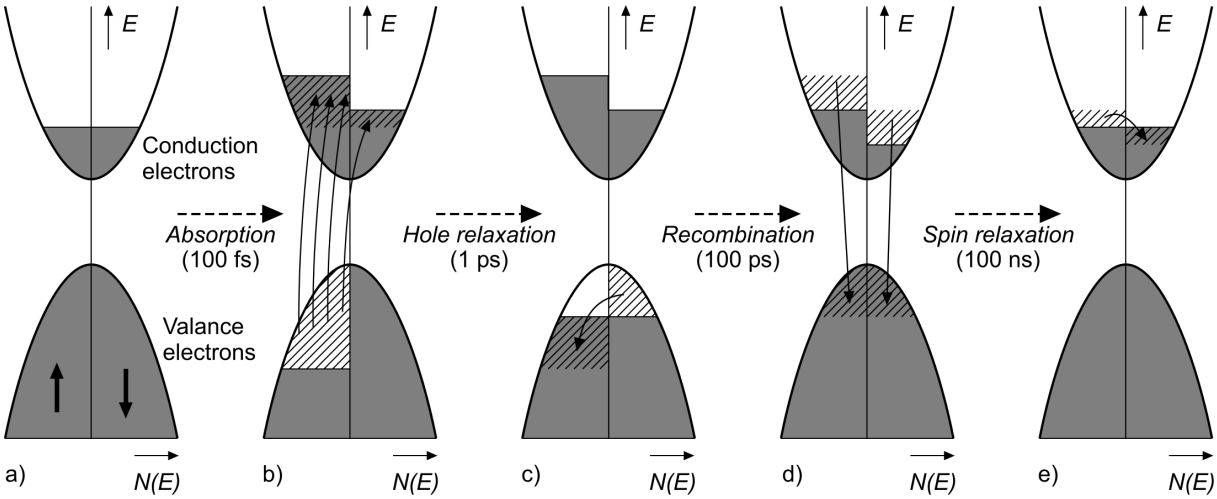

Figure 2.2: Density of states pictures showing the mechanisms after optical spin injection by a circularly polarised laser pulse of 100 fs at low temperature. Excitation by absorption generates 50% spin polarised electrons and 100% spin polarised holes (a to b). Hole relaxation levels the spin of the holes (c), after which recombination fills the holes with electrons (d). The spin polarisation of the conduction electrons remains until these are relaxed as well (e).

Absorption

A photon with an energy larger than the band gap $h\omega > E_g$ can excite an electron from the valance band into the conduction band, under conservation of energy and (angular) momentum. As the momentum of a photon is negligible compared to that of an electron, the k-vector of an excited electron is not allowed to change. However, angular momentum m_j does change, because a photon has orbital quantum number ±1, corresponding to either left or right circularly polarised light. When the photon energy used is less than that is required for exciting electrons from the split-off band, only the transitions summarised in table **2.2** are possible. These are called the optical selection rules.

Table 2.2: Optical selection rules for excitation by polarised photons.

initial band	m_j initial	Δm photon	m_j final	probability
heavy hole	-3/2	+1	-1/2	3/4
light hole	-1/2	+1	+1/2	1/4
heavy hole	+3/2	-1	+1/2	3/4
light hole	+1/2	-1	-1/2	1/4

For each photon spin state Δm two transitions are possible, each having a certain probability. When exciting with multiple photons having the same spin, e.g. a left-handed circularly polarised laser pulse, 75% of the electrons will finish in a state with spin up and 25% with spin down. The excited electrons have thus a spin polarisation of 50%, while the remaining holes have a spin polarisation of 100%. Shortly after excitation, the electrons in the valance and conduction band will thermalise, losing their excess energy $h\omega$ - E_g. The situation that is then created is shown in figure **2.2**b.

Hole spin relaxation

Due to spin-orbit coupling, holes will relax their spin very fast, typically in less than 1 ps[8]. Each collision of a valance electron with a phonon causes the orbital momentum to change, to which the total angular momentum is coupled. Therefore, the hole relaxation time is in the order of the momentum scattering time of electrons. Because of this fast relaxation process, the orbital momentum of holes is not of great importance when considering optical spin injection in GaAs. The situation for relaxed holes is shown in figure **2.2**c.

Electron-hole recombination

After electron-hole pairs are created by the photon pulse, they will recombine. There are different types of recombination processes in semiconductors: radiative, Shockly-Read-Hall and Auger recombination. When optical injection is done at a temperature of 5 K, which is the case for the experiments done for this thesis, radiative recombination dominates. Radiative recombination occurs when an electron and a hole have found each other and have formed an exciton. Excitons energies are in the order of 4 meV[11], thus only at low thermal energy ($k_BT < 4$ meV) they can be formed effectively. Therefore, recombination times at a temperature of 5 K are relatively short, in the order of 100 ps for the device with which experiments have been done.

For recombination, the same selection rules as for excitation are valid, with initial and final states exchanged in table **2.2**. However, because of the short hole relaxation time, the hole spin will remain neutrally polarised during recombination. Therefore, the rate at which spin up (down) conduction electrons with density $n_{\uparrow(\downarrow)}$ recombine can be defined as

$$\frac{\partial}{\partial t} n_{\uparrow(\downarrow)} = -R\left(n_{\uparrow(\downarrow)} p - \frac{1}{2} n_i^{\,2} \right) \tag{2.3}$$

with R a recombination proportionality constant, p the hole concentration and n_i the electron concentration for intrinsic GaAs. The recombination rate is thus proportional to the spin up (down) electron

density and the hole density. Recombination stops when electron and hole concentrations have reached equilibrium, when $\left(n_\uparrow + n_\downarrow\right) p = n_i^2$. However, at a high excitation density this last factor will be negligible.

Each recombined electron results in a recombined hole, thus the rate of change for holes is related to (2.3) as

$$\frac{\partial}{\partial t} p = \frac{\partial}{\partial t} n_\uparrow + \frac{\partial}{\partial t} n_\downarrow . \tag{2.4}$$

After excitation by a circularly polarised laser pulse, $n_\uparrow > n_\downarrow$ due to the optical selection rules. Spin up electrons will thus recombine at a higher rate than spin down electrons. Therefore, when the excitation density has the same order of magnitude or is larger than the equilibrium carrier density, the spin density $n_\uparrow - n_\downarrow$ will diminish by recombination.

Recombination in the optical injection process will result in an occupation of density of states like in figure **2.2**d.

Electron spin relaxation

Electron spin relaxation is the last process taking place after absorption of the laser pulse and before regaining equilibrium. There are several theories about the physical process causing electron spin relaxation, of which the so-called Elliot-Yafet (EY) and D'Yakonov-Perel (DP) mechanisms are most important for *n*-GaAs at temperatures near 5 K[3]. The first theory involves spin-orbit interactions resulting in spin flip at momentum scattering, while the latter depends on spin precession in between the collisions. The rate at which this relaxation process takes place is expressed using the spin relaxation time τ_s:

$$\frac{\partial}{\partial t} n_{\uparrow(\downarrow)} = -\left(+\right)\frac{n_\uparrow - n_\downarrow}{\tau_s} . \tag{2.5}$$

Figure **2.3** gives an overview from literature[12] of spin lifetimes as a function of doping concentration for *n*-GaAs at low temperature. Spin relaxation times are largest between doping levels of $2 \cdot 10^{15}$ to $5 \cdot 10^{16}$ cm^{-3}.

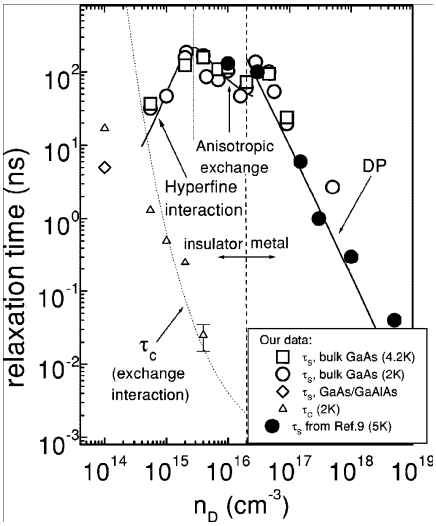

Figure 2.3: Spin relaxation time as a function of donor concentration in *n*-GaAs at low temperature.

2.3 Spin transport and precession

Once spin has been injected into the conduction band of a semiconductor, it is subject to transport mechanisms like diffusion and drift. Diffusion will cause a spreading in spin density when there is a spatial inhomogeneity, while drift moves the spin in an externally applied electric field. These two mechanisms are combined in the following partial differential equation for electron spin density as the first and second part right of the equation sign[13]:

$$\frac{\partial}{\partial t}\left(n_{\uparrow}-n_{\downarrow}\right)=D_s\nabla^2\left(n_{\uparrow}-n_{\downarrow}\right)+\mu_s\mathbf{E}\cdot\nabla\left(n_{\uparrow}-n_{\downarrow}\right) \tag{2.6}$$

where D_s is the spin diffusion constant, **E** the local electric field and μ_s the spin mobility. Now $n_{\uparrow(\downarrow)}$ is a function of space and time.

In the absence of holes, i.e. after electron-hole recombination in an *n*-type semiconductor, the spin diffusion and drift is supposed to be identical to electron diffusion and drift, $D_s \sim D_e$ and $\mu_s \sim \mu_e$. However, when holes are present the Coulomb interaction between electrons and holes influences diffusion and mobility. In *n*-GaAs, the diffusion constant of electrons is about 200 cm^2s^{-1}, 20 times bigger than the diffusion constant of holes which is 10 cm^2s^{-1}[11]. Electrons will try to move away but are slowed down by the electric field of the lagging holes. In this situation, charge transport is defined by the ambipolar diffusion D_a and mobility μ_a constants[14]:

$$D_a=\frac{n\mu_e D_h+p\mu_h D_e}{n\mu_e+p\mu_h} \tag{2.7}$$

$$\mu_a=\frac{(n-p)\mu_e\mu_h}{n\mu_e+p\mu_h} \tag{2.8}$$

with n (p) the electron (hole) concentration, D_h the hole diffusion constant and μ_h the hole mobility. Electrons and thus spin will move with these ambipolar constants.

Spin polarised electrons will react to a magnetic field as well. An externally applied magnetic field **B** can be used to create a torque $\boldsymbol{\tau}$ on the spin polarised electrons in the sample with angular momentum $\boldsymbol{\mu}$:

$$\boldsymbol{\tau} = \boldsymbol{\mu} \times \mathbf{B} \tag{2.9}$$

causing the electrons to precess around the direction of the field. The frequency ω_L with which the electrons precess is called the Larmor frequency and is defined by the gyromagnetic ratio γ:

$$\omega_L = -\gamma B = +g\frac{e}{2m_e}B \tag{2.10}$$

with B the magnitude of the magnetic field, e the electron charge, m_e the effective mass of the electron and g the Landé-factor of the electrons[15].

2.4 Optical spin detection

This section describes how spin polarised electrons in a semiconductor can be detected optically. There are two methods that can give information on the spin density in the conduction band. The first uses photoluminescence, measuring the radiation that is emitted during recombination. This light will have some degree of circular polarisation, proportional to the spin density. However, in this thesis the magneto-optic Kerr effect is used to detect spin polarised electrons locally.

Magneto-optic Kerr effect

The magneto-optic Kerr effect is the change in polarisation of light when it is reflected at the surface of a magnetised sample. This polarisation change originates in the difference in absorption for left and right circularly polarised light in a spin polarised sample. This difference is defined by the occupied and available states from which or to which electrons are excited. For an electron spin polarised *n*-doped semiconductor, the effect is shown in figure **2.4**. When probing the material with photons having the energy indicated in the figure, the presence of spin up electrons in the conduction band prevent the left circularly polarised photons to be absorbed, whereas right circularly polarised photons are allowed to excite electrons from the valance band.

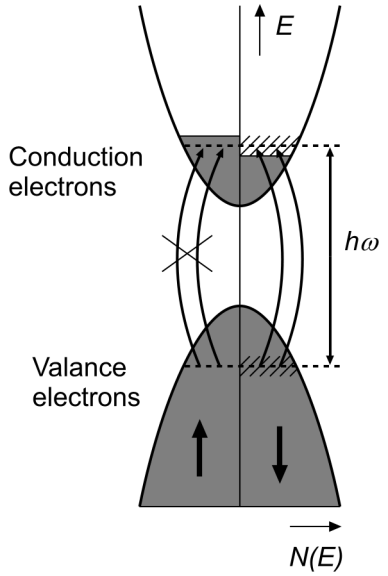

Figure 2.4: Spin dependent absorption causing the magneto-optic Kerr effect. Left circularly polarised light with the indicated energy cannot be absorbed, while right circularly polarised light can.

In optics, the influence of this asymmetrical absorption on the electromagnetic field of light is incorporated in the dielectric tensor **ε**. Therefore the magneto-optic complex constant Q is added to an isotropic tensor in Cartesian coordinates:

$$\boldsymbol{\varepsilon} = N^2 \begin{pmatrix} 1 & iQ_z & -iQ_y \\ -iQ_z & 1 & iQ_x \\ iQ_y & -iQ_x & 1 \end{pmatrix} \tag{2.11}$$

where N is the (complex) refractive index and $Q_{x,y,z}$ are the three components of Q.

The constant Q is a physical response function of the photon energy, the imaginary part representing energy absorption. Because the absorption occurs only at a specific photon energy, it will show a narrow peak in the energy spectrum for that value. Via the Kramers-Krönig relations, its real part can then be defined. An example of such behaviour is shown in figure **2.5**.

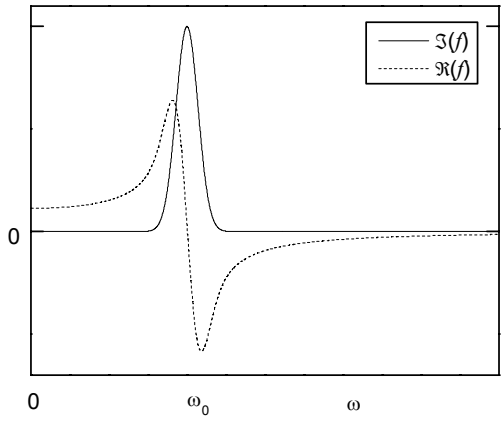

Figure 2.5: Kramers-Krönig behaviour of the real and imaginary part of a response function near a resonance frequency ω_0.

Now we will investigate the simple situation with a homogeneous dielectric tensor, a small magneto-optical constant ($Q \ll 1$) and light propagating in the *z*-direction. The quantisation axis of electron spin, also in the *z*-direction defines *Q* to have that direction as well. The complex refractive index *N* is then defined for left (*L*) and right (*R*) circularly polarised light independently[16]:

$$N_{L(R)} = N\left(1 - (+)\frac{1}{2}Q\right). \tag{2.12}$$

The reflection of a material with these refractive indices is determined by the complex reflectivity coefficient $r_{L(R)}$, differing for left and right polarisation:

$$r_{L(R)} = \frac{1 - N_{L(R)}}{1 + N_{L(R)}}. \tag{2.13}$$

When probing a material with linearly polarised light, which actually is a summation of left and right circularly polarised light (see figure **2.6**), the reflectivity coefficients r_L and r_R will induce rotation θ' and ellipticity θ'' by changing the two components differently. These effects can be described quantitatively as

$$\theta' + \mathrm{i}\,\theta'' = \frac{r_L - r_R}{r_L + r_R} \tag{2.14}$$

resulting in a description of Kerr rotation and ellipticity.

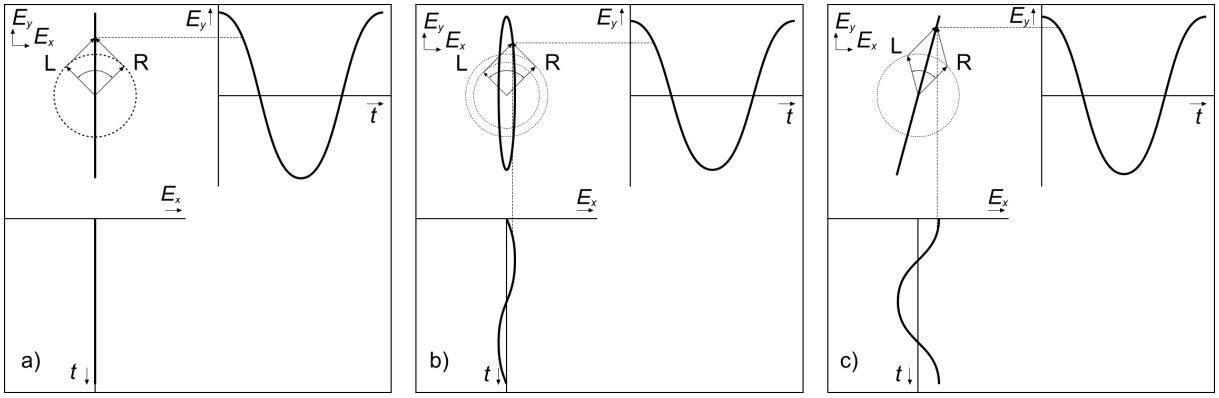

Figure 2.6: Left (L) and right (R) polarised light combine to linearly polarised light (a). When the amplitude of one component changes, ellipticity is induced (b). When the phase of one component changes, rotation is induced (c).

Multilayers

When multiple layers with different refractive indices and magneto-optical constants are involved, the magneto-optic Kerr effect can be calculated using *medium boundary matrices* and *medium propagation matrices*, taking into account multiple reflections at each interface between consecutive layers[16]. These matrices must be formed for each layer. They are then combined into one matrix that defines the relations between incident, reflected and transmitted light, as if the sample consisted of one homogeneous layer. The Kerr effect among others can then be determined for the complete system of layers. While varying some parameters, for example the wavelength of light, the thickness of a layer or the magneto-optical constant of some layers, the consequences for the Kerr effect can be determined.

To explain how these matrices work, two vectors are defined. The vector **P** contains the two components of the electromagnetic wave of a probing (laser) beam in both incident and reflected directions:

$$\mathbf{P} \equiv \begin{pmatrix} E_s^i \\ E_p^i \\ E_s^r \\ E_s^i \end{pmatrix} \tag{2.15}$$

where $E_s^{\,i}$ and $E_p^{\,i}$ are the *s*- and *p*-components of the field of the incident beam, while $E_s^{\,r}$ and $E_p^{\,r}$ are that of the reflected beam going in the other direction. In figure **2.7** these definitions are indicated. A second vector **F** contains the electric field $E_{x(y)}$ and magnetic field $H_{x(y)}$ in the plane of the medium boundary between two layers:

$$\mathbf{F} \equiv \begin{pmatrix} E_x \\ E_y \\ H_x \\ H_y \end{pmatrix}. \tag{2.16}$$

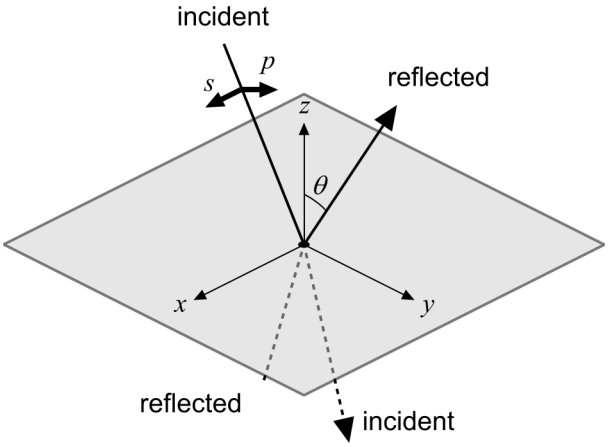

Figure 2.7: Definitions of the *x*-, *y*-, *s*- and *p*-directions at a medium boundary.

The 4x4 medium boundary matrix **A** defines the relation between these two vectors as

$$\mathbf{F} = \mathbf{A} \cdot \mathbf{P} \,. \tag{2.17}$$

At the interface between two layers, numbered 1 (above) and 2 (under), the vector **F** must be continuous, i.e. $\mathbf{F}_{1,b} = \mathbf{F}_{2,t}$ where the subscript *b* (*t*) denotes the bottom (top) of the layer. This implies that $\mathbf{A}_1 \cdot \mathbf{P}_{1,b} = \mathbf{A}_2 \cdot \mathbf{P}_{2,t}$ where $\mathbf{P}_{1,b}$ describes the beam at the bottom of layer 1 and $\mathbf{P}_{2,t}$ describes the beam at the top of layer 2.

The next step is to determine the evolution of the incident and reflected beams when travelling in a medium. Because of this, the medium propagation matrix **D** is built. If $\mathbf{P}_{2,t}$ describes the beam at the top of layer 2 and $\mathbf{P}_{2,b}$ describes it at the bottom, the propagation matrix $\mathbf{D}_2$ for that layer relates them as:

$$\mathbf{P}_{2,t} = \mathbf{D}_2 \cdot \mathbf{P}_{2,b} \tag{2.18}$$

Going from the bottom of layer 1 to the top of layer 3, the following construction is obtained:

$$\mathbf{F}_{1,b} = \mathbf{A}_1 \cdot \mathbf{P}_{1,b} = \mathbf{A}_2 \cdot \mathbf{P}_{2,t} = \mathbf{A}_2 \cdot \mathbf{D}_2 \cdot \mathbf{P}_{2,b} = \mathbf{A}_2 \cdot \mathbf{D}_2 \cdot \mathbf{A}_2^{-1} \cdot \mathbf{A}_3 \cdot \mathbf{P}_{3,t} \tag{2.19}$$

A visualisation for this calculation is given in figure **2.8**.

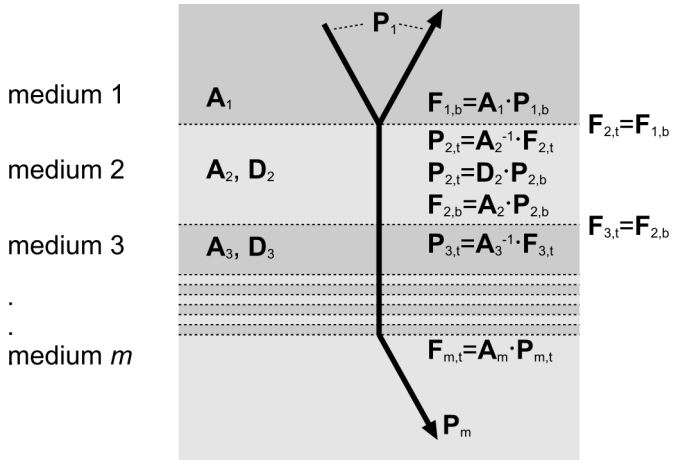

Figure 2.8: Medium boundary matrices **A** and medium propagation matrices **D** used to describe a laser beam going through different layers.

This can go on for m layers on top of each other, each with its own **A** and **D**. Finally, a matrix **M** describing the total medium is constructed such that

$$\mathbf{P}_1 = \mathbf{M} \cdot \mathbf{P}_m \tag{2.20}$$

where

$$\mathbf{M} = \mathbf{A}_1^{-1} \prod_{j=2}^{m-1} \left(\mathbf{A}_j \cdot \mathbf{D}_j \cdot \mathbf{A}_j^{-1} \right) \cdot \mathbf{A}_m \,. \tag{2.21}$$

In practice, medium 1 will be the air or vacuum in front of the sample, while medium m is the final medium which either absorbs all light or is the same as medium 1 in which case the sample is transparent.

The matrices **A** and **D** are given for an arbitrary direction of beam incidence and Q in [17]. Here they are given for the case of perpendicular incidence and Q in the z-direction:

$$\mathbf{A} = \begin{pmatrix} 1 & 0 & 1 & 0 \\ 0 & 1 & 0 & 1 \\ \frac{1}{2}\mathrm{i}NQ & -N & -\frac{1}{2}\mathrm{i}NQ & -N \\ N & \frac{1}{2}\mathrm{i}NQ & -N & \frac{1}{2}\mathrm{i}NQ \end{pmatrix} \tag{2.22}$$

and

$$\mathbf{D} = \begin{pmatrix} U\cos\delta_\mathrm{i} & U\sin\delta_\mathrm{i} & 0 & 0 \\ -U\sin\delta_\mathrm{i} & U\cos\delta_\mathrm{i} & 0 & 0 \\ 0 & 0 & U^{-1}\cos\delta_r & -U^{-1}\sin\delta_r \\ 0 & 0 & U^{-1}\sin\delta_r & U^{-1}\cos\delta_r \end{pmatrix}. \tag{2.23}$$

In these matrices, N is the refractive index, Q the magneto-optical constant, $U = \exp\left(-\mathrm{i}\frac{Nd}{2\pi\lambda}\right)$, $\delta_\mathrm{i} = \frac{Nd}{4\pi\lambda}Q$, $\delta_r = -\frac{Nd}{4\pi\lambda}Q$, d the thickness of a layer and λ the wavelength of light.

Because the complete interaction between incident, reflected and transmitted beams is defined in the matrix **M**, the reflection and transmission coefficients can be calculated. Because of this, the 4x4 matrix **M** is split into four 2x2 matrices **G**, **H**, **I** and **J** so that incident *i*, reflected *r* and transmitted *t* light are related as

$$\begin{pmatrix} E_s^i \\ E_p^i \\ E_s^r \\ E_p^r \end{pmatrix} = \begin{pmatrix} \mathbf{G} & \mathbf{H} \\ \mathbf{I} & \mathbf{J} \end{pmatrix} \cdot \begin{pmatrix} E_s^t \\ E_p^t \\ 0 \\ 0 \end{pmatrix} \tag{2.24}$$

where the boundary condition is set such that there is no reflected beam coming from the other side of the sample. The reflected beam can now be directly related to the incident beam:

$$\begin{pmatrix} E_s^r \\ E_p^r \end{pmatrix} = \mathbf{I} \cdot \mathbf{G}^{-1} \cdot \begin{pmatrix} E_s^i \\ E_p^i \end{pmatrix} \tag{2.25}$$

so that $\mathbf{I}\cdot\mathbf{G}^{-1}$ is the reflection matrix:

$$\mathbf{I} \cdot \mathbf{G}^{-1} = \begin{pmatrix} r_{ss} & r_{sp} \\ r_{ps} & r_{pp} \end{pmatrix} \tag{2.26}$$

With these relations known, the Kerr rotation θ' and ellipticity θ'' for s-polarised light can easily be expressed as

$$\theta' + \mathrm{i}\,\theta'' = \frac{r_{sp}}{r_{ss}} \tag{2.27}$$

which is the same for *p*-polarised light in the case of perpendicular incidence.

3 All-electrical Spin Injection and Detection Device

The purpose for the all-electrical spin injection and detection device discussed here is making a magnetoresistance (MR) based on a semiconductor channel. A simplified drawing of it has already been shown in figure **1.3**. The device uses two tunnel barriers placed laterally on a GaAs spin transport channel, each with a ferromagnetic electrode on top of it. One is used for spin injection, the other for spin detection. The total resistance of the device, from one electrode to the other, depends on the relative magnetisation of the electrodes, being either parallel or antiparallel.

In this chapter the design of the device is being discussed. While the focus will be on the spin transport layer, for which the work in the rest of this thesis has been done, electrical spin injection and detection will be explained first. Next, all components of the design will be shown, then the carrier distribution is calculated for the spin transport channel.

3.1 Electrical spin injection and detection

Electrical spin injection and detection use a tunnel barrier between a ferromagnetic layer and an *n*-doped semiconductor to create an asymmetrical tunnelling probability of spin up and spin down electrons. Schematically, this is shown in figure **3.1**.

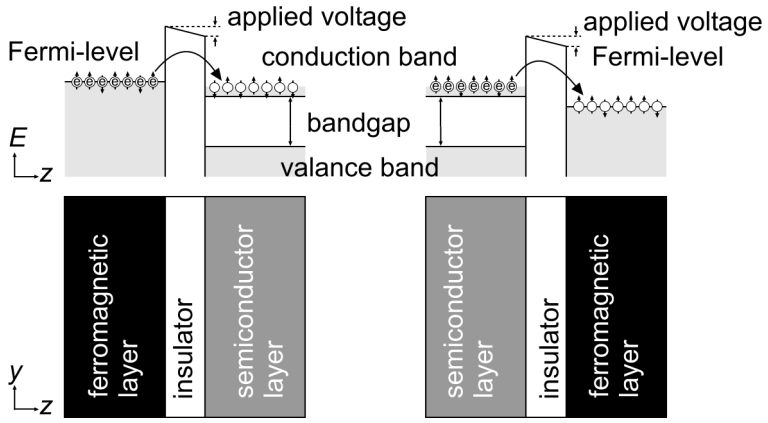

Figure 3.1: Electrical spin injection into (left) and spin detection from (right) a non-magnetic semiconductor layer using an insulator as a tunnel barrier and a ferromagnetic layer.

When electrons tunnel from a ferromagnetic layer through an insulator into a semiconductor, the tunnelling probability for each spin channel is proportional to the density of states at the Fermi-level on both sides of the barrier[18]. At this energy level, the occupied states of the layer tunnelling from and the available states tunnelling to are defined with $N_{\uparrow(\downarrow)}(E_F)$. In the ferromagnetic layer, there is an imbalance of the spin up and spin down density at the Fermi level: $N_{\uparrow}(E_F) > N_{\downarrow}(E_F)$, while in the semiconductor the density of states are equal. In the picture, this is indicated by a majority of spin up electrons on the left side of the injection tunnel barrier. On the right side, the vacant places are equally distributed between spin up and spin down. This causes the current from the ferromagnetic layer into the semiconductor to be spin-polarised, injecting spin polarisation in the semiconductor.

Note that without the tunnel barrier, spin injection into the semiconductor will be negligible due to the conduction mismatch. The resistance of the semiconductor, identical for both spin channels, is much greater than the spin selective resistance in the ferromagnetic layer. The net current is thus dominated by the conductivity of the semiconductor and thus the current is neutrally polarised. With a tunnel junction, the resistance is dominated by the spin selective tunnel barrier, unbalanced for the separate spin channels. This makes it possible to have a larger spin up electron current than spin down electron current.

For spin detection, electrons tunnel from the semiconductor to the spin up polarised ferromagnetic layer. Now spin polarisation in the semiconductor plays a role as well. When the electrons are polarised with spin up in the conduction band, the probability for tunnelling of spin up electrons is much greater than that of spin down electrons. On the other hand, if the semiconductor has a spin down polarisation, the combined tunnelling current of spin up and spin down electrons is smaller. The resistance of the spin detection tunnel junction is thus dependent on the spin polarisation in the semiconductor.

As a spin injection tunnel barrier, an insulator can be used like AlO_x, but the natural Schottky-barrier that is created by growing a metal layer on a semiconductor can be exploited as well. Defining the width of the tunnel barrier is more difficult then, because the doping concentration in the top layer of the semiconductor, directly under the interface with the ferromagnetic layer, must be tuned.

3.2 Design by IMEC

The functionality of the all-electrical spin injection and detection device is based on the long electron spin relaxation time in *n*-doped GaAs and the spin injection and detection techniques using a tunnel barrier as described in section 3.1. The spin lifetime in *n*-GaAs is longest with a doping of $2 \cdot 10^{15}$ - $5 \cdot 10^{16}$ cm^{-3} and can be up to 100 ns at 5 K (see figure **2.3**). In the past, electrical spin injection in *n*-GaAs has already been detected optically using spin-LEDs[19] and the magneto-optic Kerr effect[20].

IMEC Leuven has focused on making small sub-micrometer structures to minimise loss of spin polarisation during the transport of electrons. Their device, for which the cross-section is shown in figure **3.2**, uses a 0.5 mm thick layer of intrinsic GaAs as a substrate. On top of that, a 200 nm layer of $Al_{0.3}Ga_{0.7}As$ is grown, having a higher band gap than (*n*-)GaAs. A Si δ-doping of $2 \cdot 10^{11}$ cm^{-2} is applied in this layer 10 nm below the top. Then the 200 nm thick *n*-GaAs spin transport channel with a silicon

doping of $5 \cdot 10^{16}$ cm^{-3} is grown. The δ-doping pulls electron carriers to the bottom of the channel where the AlGaAs barrier blocks them. The electron density at the top surface of the spin transport channel is increased by two 6 nm thick highly doped *n*+(+)-GaAs layers, having a doping level of $7 \cdot 10^{18}$ and $1.5 \cdot 10^{19}$ cm^{-3}. A layer of 1.5 nm insulating AlO_x is then grown, on top of which two 250 nm wide 5 nm thick CoFe ferromagnetic electrodes are grown, spaced 500 nm apart. One electrode is used for electrical spin injection, while the other detects the spin. To allow this, the AlO_x layer is used as a tunnel barrier.

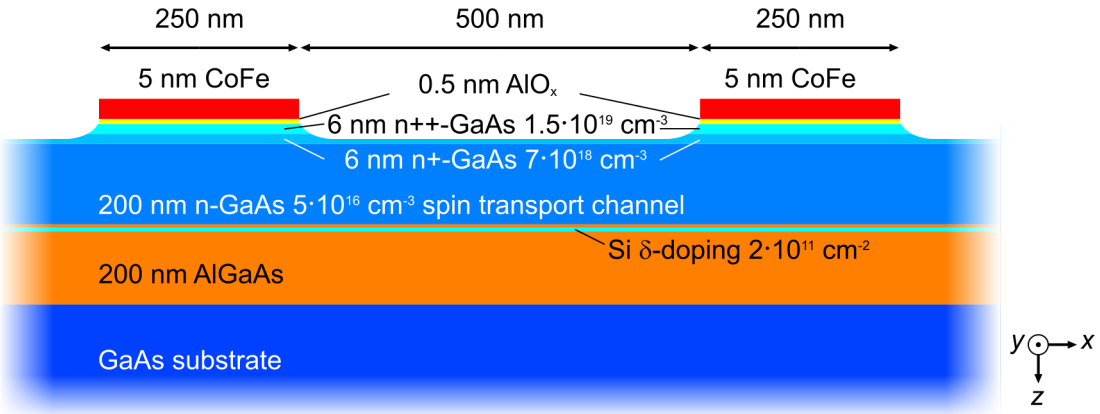

Figure 3.2: Cross-section of IMEC design for the all-electrical spin injection and detection device.

To the left and right of the electrodes, out of view in figure **3.2**, ohmic contacts are grown on the channel. These contacts allow an electron current directly into or out of the conduction band of the channel. They make testing of a single tunnel barrier possible or can create a well defined current in the transport channel. In figure **3.3**, a microscopic top view of the device is shown, showing the ferromagnetic electrodes, the ohmic contacts and the spin transport channel. The electrodes have their easy axis in the long (*y*-)direction.

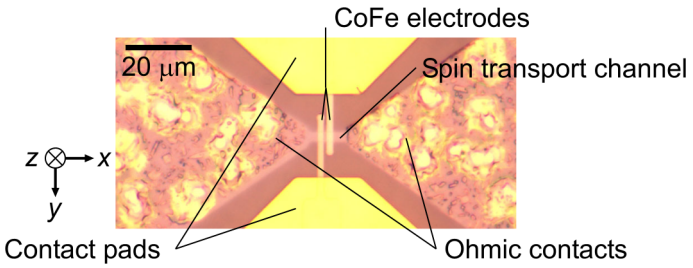

Figure 3.3: Microscopic picture of the lateral layout of the all-electrical spin injection and detection device.

Spin transport channel

The carrier concentrations and electric fields in the heterostructure as a function of depth are of great importance when engineering an all-electrical spin injection and detection device. The spin transport channel should be designed such that carrier concentration is optimal for a long spin lifetime. Meanwhile, spin injection and detection with the tunnel barriers must be effective and the path length be-

tween the two electrodes must be chosen sufficiently small such that spin polarisation is not lost when electrons are transported from one to the other. One crucial parameter is the thickness of the highly doped top layers, to which the carrier concentration is extremely sensitive as will be shown below. They are needed to compensate for *Fermi level pinning*, a phenomenon in which the surface states of a semiconductor deviate from the periodic Bloch potential. The Fermi level of the *n*-GaAs semiconductor is pinned halfway the conduction and the valance band, creating a carrier depletion region where electrons have diffused to deeper layers.

The devices are constructed by first depositing the complete (Al)GaAs heterostructure including the highly doped top layers on the intrinsic GaAs substrate. Aluminium is then added and oxidised, after which the CoFe contacts are deposited. Finally, the AlO_x covered GaAs surface between the contacts is etched away, the duration controlling the final thickness of these top layers. Because an exact relation between etching time and layer thicknesses is hard to give, there remains some uncertainty in the carrier concentration near the top of the transport channel.

3.3 Band diagram calculation

The band diagram has been calculated for room temperature using dedicated simulation software (SimWindows). This has been done for various top layer thicknesses in order to make their influence visible. In figure **3.4**, the results for these simulations are shown. The conduction and valance band are given together with conduction electron concentrations as a function of z in the sample. Here, $z = 0$ is defined as the top of the 200 nm spin transport channel. The n+(+) top layers lie at $z < 0$ while the AlGaAs buffer is situated at $200 < z < 400$ nm. This is indicated in the figure. Each line represents different top layer thicknesses, line 1 denoting no n+(+) layers at all, 2 with only the first layer of $7 \cdot 10^{18}$ cm^{-3} and lines 3 to 6 represent a growing second layer of $1.5 \cdot 10^{19}$ cm^{-3}.

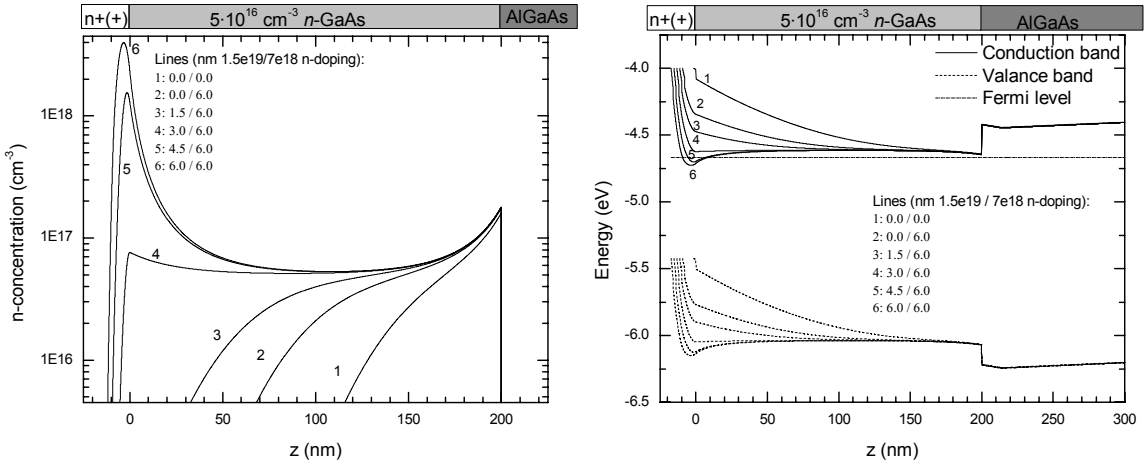

Figure 3.4: Conduction band electron concentration (left) and band diagram (right) near the transport channel at room temperature as a function of z for the all-electrical spin injection and detection device. Lines 1 to 6 represent growing n+(+) layers from none to 6 nm of $7 \cdot 10^{18}$ cm^{-3} and 6 nm of $1.5 \cdot 10^{19}$ cm^{-3}.

In the figure, several features can be seen. At the *n*-GaAs/AlGaAs interface, a peak in carriers is caused by the δ-doping layer in the AlGaAs at $z = 210$ nm. The δ-doping layer pulls the electrons to the *n*-GaAs/AlGaAs. As a result, the conduction band electron density peaks at $2 \cdot 10^{17}$ cm^{-3} between $190 < z < 200$ nm. At the other end of the channel near $z = 0$, the great influence of varying the top layer thicknesses can clearly be seen. While they are needed to compensate for a carrier depletion in the channel, a thicker layer with doping of $1.5 \cdot 10^{19}$ cm^{-3} gives carrier concentrations far exceeding 10^{17} cm^{-3}.

From these results can be concluded that etching for a time too short or too long can result in an unfavourable carrier distribution. When the top layer exceeds 3 nm, the spin lifetime will be reduced several orders of magnitude by the electron concentration exceeding 10^{17} cm^{-3}. On the other hand, when having less than 1.5 nm of the n++ layer, the in-plane total carrier concentration in the device is reduced significantly. The electrical resistance of the device will be higher and transport of spin polarised electrons from one electrode to the other will be more difficult.

The strong non-homogeneity of the band diagram is a consequence of the small thickness of the transport layer of 200 nm. While it minimises the spin transport distance, the physical processes inside are more difficult to predict. Spin relaxation is strongly related to electron density and electron energy. Additionally, later on in this thesis it will be shown that the non-homogeneity complicates optical studies of the device.

Note that the simulations have been performed at room temperature, due to limitations in the simulation software. Later on situations at low temperature are discussed. The general features of the band diagram and the carrier concentration at a temperature of 5 K is not expected to differ much though.

4 TiMMS

A technique to explore spin dynamics with a very high temporal resolution is *TiMMS* (Time-resolved Magnetization Modulation Spectroscopy). Using laser pulses spin is first optically injected and then detected by a part of the same pulse, delayed 0 - 2000 ps. This technique is described here and applied for the spin transport channel of the all-electrical spin injection and detection device of the previous chapter.

4.1 TiMMS Setup

TiMMS uses very short laser pulses to optically inject and detect spin polarised electrons in a sample. Each laser pulse is split into a *pump* and a *probe*. While the pump pulse generates a local spin polarisation, the probe pulse is delayed before detecting them. The spin polarised electrons in the sample can be monitored over up to 2 ns with a temporal resolution of 120 fs. The complete setup used for this measurement technique is drawn in figure **4.1**, its components are explained below.

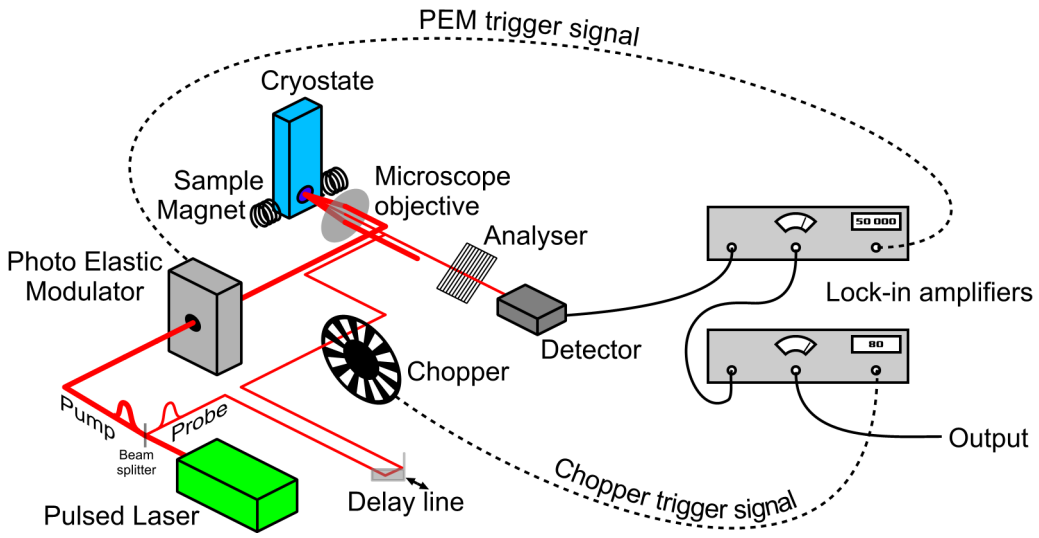

Figure 4.1: Drawing of the TiMMS setup. A laser generates pulses, which are split into a pump and a probe. The pump generates spin-polarised electrons at the sample where they are detected with the probe. An analyzer gives signal to the detector. The signal is modulated by a PEM and a chopper and amplified with two lock-in amplifiers.

The laser pulses are generated with a Ti:sapphire laser at a repetition rate of 80 MHz. The wavelength of the laser is tuneable, as well as the pulse length. Compared to continuous lasers, the wavelength is

not well defined. As a consequence of Fourier transformation, the full-width-half-maximum (FWHM) of the laser energy bandwidth $\Delta\omega_p$ and the FWHM of the pulse duration τ_p are coupled by[21]:

$$\Delta\omega_p \tau_p \geq 2\pi C_B \qquad (4.1)$$

where C_B is a constant dependent on the pulse shape. For a Gaussian pulse, $C_B = 0.44$. A typical pulse duration of 120 fs thus results in a bandwidth of 8 nm at a laser wavelength of 800 nm.

A beam splitter divides each laser pulse into a pump and a probe, following different paths in the TiMMS setup. The pump, polarised at 90°, first passes through a *Photo Elastic Modulator* (PEM). The PEM consists of a crystal having two optical axes of which one has a tuneable refractive index, controlled by an externally applied alternating electric field. Placed under an angle of 45°, it modulates the light between left and right circularly polarised at a frequency f_{PEM}. The benefit of this modulation is explained below. Note that the frequency will be much lower than the repetition rate of the laser, thus for each pump pulse the PEM appears to be static.

The probe pulse is delayed relative to the pump using a *delay line* consisting of a beam reflector moveable on rails. It can change the path length of the probe and thus controls the difference in time of arrival between pump and probe at the sample location via the speed of light. The beam reflector is moveable over 30 cm corresponding to a time shift of $\Delta t = 2$ ns.

Pump and probe are focused on the sample using a microscopic objective as shown in figure **4.2**. As long as both beams are parallel to each other, they will create overlapping spots on the sample surface. The beams are reflected here and exit the objective, again as parallel bundles. While the pump beam is blocked, the probe continues its way to an optical detector.

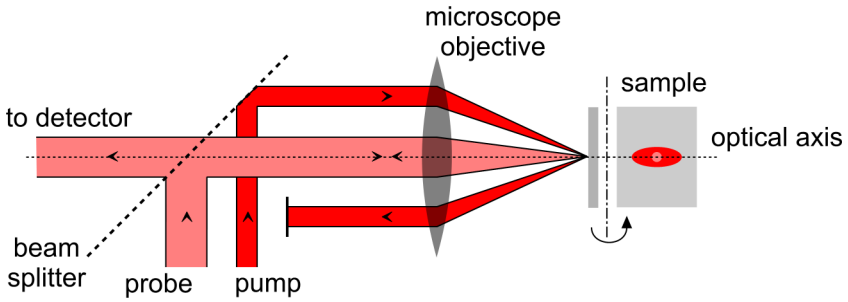

Figure 4.2: Schematic illustration of the paths of pump and probe near the sample. They pass parallel through an objective, being focussed on the sample. The reflection of the pump is blocked.

The size of the pump and probe spot on the sample is determined by the numerical aperture of the microscope objective and the part of the aperture that is covered by the laser beam. The wider the laser beam is when entering the objective, the smaller the spot that it creates. The pump spot created with the setup of figure **4.2** will thus be larger than the probe spot.

An analyser consisting of a quarter wave plate and a polariser that are placed in front of the detector allows detection of either rotation or ellipticity in the reflected probe beam. Therefore, the modulation by the PEM and a lock-in amplifier are used. This will be explained below using Jones vector representation.

Because some scattering of the pump beam will always be present in the detector signal, the probe is modulated with a chopper blocking the light at a frequency $f_{\mathrm{chop}} << f_{\mathrm{PEM}}$. This allows distinguishing signal originating in the probe and pump with a second lock-in amplifier.

In our TiMMS setup, the sample is positioned on a cold finger in a liquid helium cooled cryostat, allowing performing measurements at low temperatures. Furthermore, an electromagnet can apply a magnetic field in the sample. This field can be used to magnetise the ferromagnetic electrodes of our sample or to let spin polarised electrons exhibit Larmor precession.

Jones vector representation

The modulation between left and right circularly polarised light of the PEM causes the spin polarisation in the sample to be modulated between up and down. The linearly polarised probe is affected by this spin, rotating its reflection via the magneto-optic Kerr effect as defined by equation (2.14) or (2.27). For small rotation θ' and ellipticity θ'', the reflected probe beam can be represented as the following Jones vector containing the same modulation frequency:

$$\mathbf{P}_{probe} = E_0 \begin{pmatrix} 1 \\ (\theta' + \mathrm{i}\theta'')\cos(f_{\mathrm{PEM}} t) \end{pmatrix} \tag{4.2}$$

where E_0 is the amplitude of the electromagnetic field. The magnitude of θ' and θ'' will depend on the spin polarisation that is still present in the sample after a delay time Δt relative to the pump pulse.

The analyser can be set in two modes by turning the polariser to an angle of either 90° or 45° relative to the probe polarisation, while the quarter-wave plate is set at a fixed angle of 45°. This can be represented with the following Jones matrices:

$$\mathbf{A}_{\mathrm{ell}} = \mathbf{P}_{45} \cdot \mathbf{Q}_{45} = \frac{1}{2}\begin{bmatrix} 1 & 1 \\ 1 & 1 \end{bmatrix} \cdot \frac{1+\mathrm{i}}{2}\begin{bmatrix} 1 & -\mathrm{i} \\ -\mathrm{i} & 1 \end{bmatrix} = \frac{1}{2}\begin{bmatrix} 1 & 1 \\ 1 & 1 \end{bmatrix} \tag{4.3}$$

$$\mathbf{A}_{\mathrm{rot}} = \mathbf{P}_{90} \cdot \mathbf{Q}_{45} = \begin{bmatrix} 0 & 0 \\ 0 & 1 \end{bmatrix} \cdot \frac{1+\mathrm{i}}{2}\begin{bmatrix} 1 & -\mathrm{i} \\ -\mathrm{i} & 1 \end{bmatrix} = \frac{1+\mathrm{i}}{2}\begin{bmatrix} 0 & 0 \\ -\mathrm{i} & 1 \end{bmatrix} \tag{4.4}$$

where $\mathbf{A}_{\mathrm{ell}}$ ($\mathbf{A}_{\mathrm{rot}}$) represents the Jones matrix of the analyser in ellipticity (rotation) mode, $\mathbf{P}_{45}$ ($\mathbf{P}_{90}$) the polariser at 45° (90°) and $\mathbf{Q}_{45}$ the quarter-wave plate at 45°.

Multiplying the analyser matrix with the probe vector will result in a Jones vector representing the light entering the optical detector. The detector measures the intensity of this light. For the two modes of the analyser, in first order approximation the intensity I is either

$$I_{\mathrm{rot}} = E_0^{\,2}\left(\frac{1}{2} + \theta' \cos(f_{PEM} t)\right) \tag{4.5}$$

for the rotation mode or

$$I_{\mathrm{ell}} = E_0^{\,2}\left(\frac{1}{2} - \theta'' \cos(f_{PEM} t)\right) \tag{4.6}$$

for the ellipticity mode. The lock-in amplifier set at the modulation frequency f_{PEM} can thus either measure rotation or ellipticity in the probe signal.

Pump and probe wavelength

As mentioned in chapter 2, both optical spin injection and optical spin detection depend on the photon energy used. In semiconductors, the pump photons must have an energy slightly higher than the band gap to be able to excite electrons.

For the probe, the wavelength for which spin will be detected most effectively depends on the energy distribution of the spin polarised conduction electrons. For the low temperatures at which TiMMS experiments in this thesis have been performed, the thermal energy k_BT is very small (0.43 meV at 5 K). The energy margin at which the occupied density of states differs for spin up and spin down electrons will be of this order of magnitude. However, the spectral bandwidth of the probe pulse is much larger (typically 15 meV). The behaviour of Q will therefore be described by the convolution of the laser spectrum and a narrow Kramers-Krönig related resonance peak, as in figure **2.5**. The resonance frequency lies at the semiconductor band gap.

Using two synchronised pulsing Ti:sapphire lasers, it is possible to pump and probe with different wavelengths. Electrons can then be detected with an energy other than they are excited. This allows for experiments where the response can be measured as a function of wavelength, without changing the pump energy, or vice versa. Another advantage of using two colours is that the pump signal can be efficiently blocked using a notch filter, improving the signal to noise ratio at the detector. Consequently, the pump and probe may overlap each other when entering the microscopic objective, allowing using its full aperture, as shown in figure **4.3**. Therefore, the spatial resolution that can be obtained with two colours is improved compared to what can be realised using one colour. On the other hand, the temporal resolution will be limited by the stability of the laser repetition rate and the electronics responsible for synchronising the two lasers.

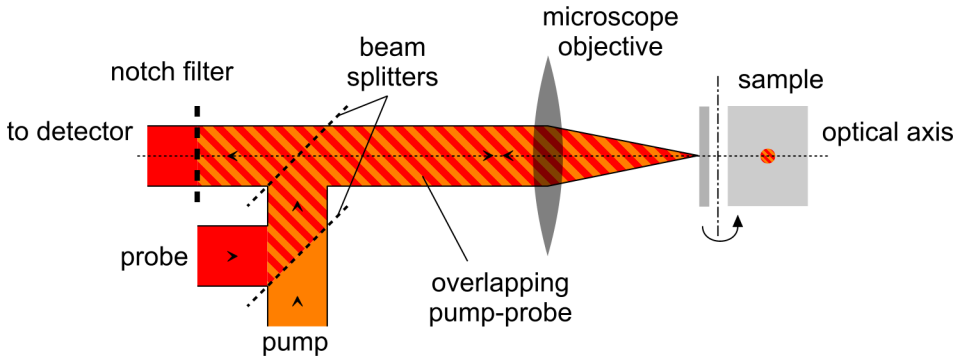

Figure 4.3: : Schematic illustration of the configuration of pump and probe paths using two beam splitters and a notch filter.

4.2 Spin lifetime

Using the setup described in the previous section with the single colour pump-probe configuration as in figure **4.2**, timescans have been made of a spin package that is injected in the spin transport channel of the device shown in figure **3.2**. Therefore, the pump-probe delay time Δt is varied between -2 and

1900 ps while measuring the spin signal. Results of a measurement without a magnetic field and one with an in-plane magnetic field of 2860 Gauss are shown in the left of figure **4.4**.

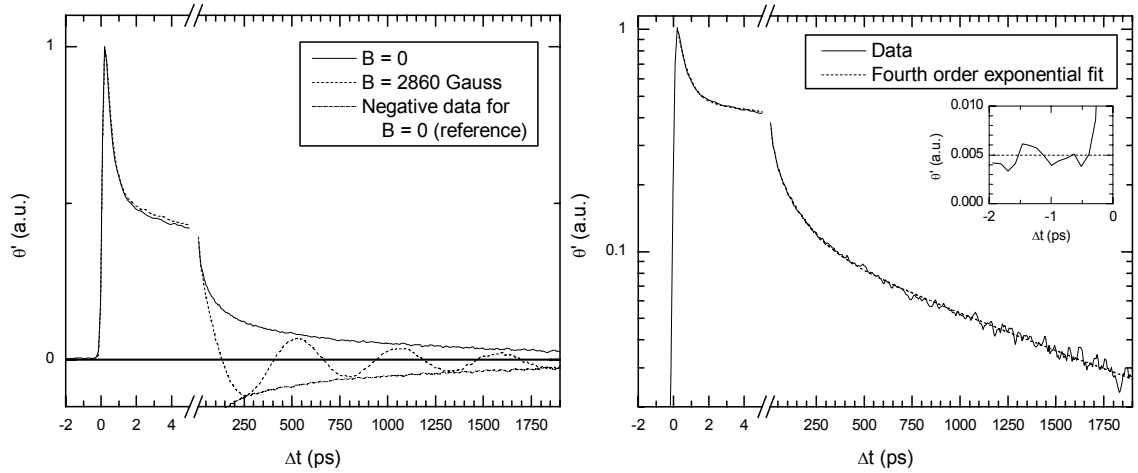

Figure 4.4: Timescans of a spin package injected at $\Delta t = 0$ in the spin transport channel with and without magnetic field (left). A fourth order exponential decay fit is needed to match the data (right).

During these measurements, the sample was cooled to a temperature of 5 K and the wavelength of the pump and probe was 810 ± 10 nm. The pump and probe were focussed to a spot with a diameter of 5 μm. Time-averaged pump and probe intensity were respectively 1.0 mW and 0.5 mW.

As can be seen from this figure, the spin signal increases suddenly at $\Delta t = 0$, where the pump and probe pulses arrive at the sample simultaneously. For increasing delay time, the signal decreases. To adequately fit the data without magnetic field, it has been empirically determined that a summation of four exponential decay functions $a_i \exp\left(-\Delta t / \tau_i\right)$ is needed. Each function has its own amplitude a_i and time constant τ_i. In the right part of figure **4.4**, the fitted function is shown on top of the data in a semi-logarithmical plot. The parameters for this function are shown in table **4.1**, together with the offset determined with the data at negative delay time, shown in the inset of the mentioned plot.

Table 4.1: Exponential function needed to fit the data in figure **4.4**.

Exponential	a (a.u.)		τ (ps)	
1	0.809	± 0.005	0.526	± 0.005
2	0.197	± 0.004	19.6	± 0.7
3	0.162	± 0.004	126	± 5
4	0.116	± 0.002	1133	± 19
offset	0.005			

An estimation can be made for the exciton density in the spin transport layer for these measurements. Therefore, the photon energy of 1.53 eV and the pulse repetition rate of 80 MHz are used to calculate the amount of photons in each laser pulse. For the pump intensity of 1.0 mW, each pulse contains $5.1 \cdot 10^7$ photons. Dividing these photons over a circular spot with radius 2.5 μm, a photon density of $2.6 \cdot 10^{14}$ cm^{-2} per pulse enters the sample from the top. For calculating the exciton density, we have to

determine how many of these photons get absorbed in the spin transport channel. Using the Fresnel equation for external reflectance R:

$$R = \left(\frac{1-n}{1+n} \right)^2$$

with n the refractive index of GaAs, the transmittance $T = 1 - R$ can be determined. For GaAs at a temperature of 5 K, $n = 3.60$[11] and thus $R = 0.32$. Consequently, $1.8 \cdot 10^{14}$ photons cm^{-2} pass through the top layer. Of those photons, $2.9 \cdot 10^{13}$ are absorbed in the 200 nm spin transport channel using the absorption coefficient of GaAs of $9 \cdot 10^3$ cm^{-1} [11] for the pump wavelength. Each absorbed photon results in an exciton, thus at the moment of spin injection, the exciton density is $1.5 \cdot 10^{18}$ cm^{-3} which is large compared to the doping density of $5 \cdot 10^{16}$ cm^{-3}.

For the four exponential decay time constants, τ_1 is considered to be the hole relaxation time because has the order of magnitude of hole spin relaxation times reported in literature[8]. Then τ_4 must be the electron spin relaxation time, as no spin signal can remain after electron spin is relaxed.

The time constants τ_2 and τ_3 cannot be interpreted as easily as the other two. Probably they are partly induced by recombination, because the excitation density is high enough to decrease the spin density by asymmetrical recombination of spin up and spin down electrons (see section 2.2). Another process responsible for the decay at these timescales could be spin diffusion, causing the spin polarised electrons flowing out of the probe spot. Furthermore, because of the high excitation density, electrons in the conduction band will be at a higher energy and thus have a higher k-value. The D'Yakonov-Perel spin relaxation mechanism is related to the electron momentum and can increase with high excitation density. Therefore, the spin relaxation rate is expected to be high at first and decrease in time, reaching its final value when the electrons have recombined with the available holes.

For the data retrieved with magnetic field, the spin can be seen precessing with a periodicity of 520 ps. The spin precesses over the full 180^o as can be seen by the minima falling over the negative data with no field, which is added for reference to figure **4.4**. Using the value of the magnetic field, the precession frequency and equation (2.10), the gyromagnetic ratio of the electrons in the spin transport channel is thus determined to a value of $6.7 \cdot 10^9$ $T^{-1}s^{-1}$.

5 Origin of Kerr reflection

In this chapter, the origin of the Kerr rotation and ellipticity will be investigated more thoroughly for the spin transport channel of the all-electrical spin injection and detection device shown in figure **3.2**. First, TiMMS timescans are generated with different probe energies. As will be shown, the Kerr effect is influenced significantly by the probe wavelength. Therefore, numerical simulations have been carried out to be able to define the Kerr effect as a function of probe wavelength and the magneto-optical constant *Q*. Using an approximation of *Q* shows similarities between the measured and simulated Kerr effects as function of probe wavelength.

5.1 Kerr effect as a function of probe energy

To be able to understand the spin relaxation processes and the interaction of spin with the probe laser beam, an experiment has been set up to investigate the dependence of the Kerr effect on the probe energy. Therefore, two-colour TiMMS experiments have been carried out, using the pump-probe configuration shown in figure **4.3**. While the pump wavelength is fixed at 780 nm, timescans have been made for several probe wavelengths. Both Kerr rotation and ellipticity have been measured as a function of delay time.

Pump and probe pulses are created by two synchronised Ti:sapphire lasers. The pump laser is set at a wavelength of 780 ± 8 nm and a time-averaged intensity of 250 μW, considering a minimum in exciton density and sufficient signal for performing measurements. A notch filter that blocks light between 760 and 780 nm with an efficiency of 10^5 is used to block the pump beam from the reflection at the sample, while the probe beam is let through. One drawback is that no probe beam with a wavelength between 760 and 780 nm can be used. The spot at the sample has a diameter of 2.5 μm. The analyser in front of the detector is set to measure either rotation or ellipticity, while the wavelength of the probe beam is set to several values. After each wavelength adjustment, the time averaged intensity of the probe is set to 1.2 mW, so that sufficient signal is being measured.

The results for the TiMMS timescans are shown in figure **5.1**, with separate graphs for rotation and ellipticity. Note the absence of the first peak between 0 and 2 ps, which is present in the one-colour measurement in section 4.2. This can be dedicated to the lower temporal resolution of the two colour pump-probe technique. However, this is not a problem for the rest of the timescan.

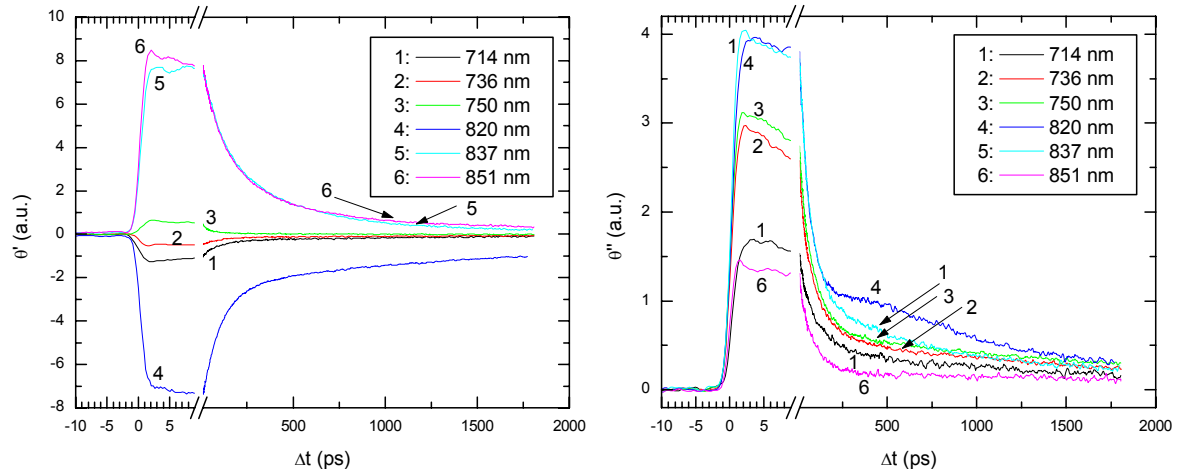

Figure 5.1: Rotation θ' (left) and ellipticity θ'' (right) timescans for various probe wavelengths with a pump wavelength of 780 nm.

In figure **5.2**, the signal at several pump-probe delay times is given. This shows the wavelength dependency of the Kerr effect in a glance.

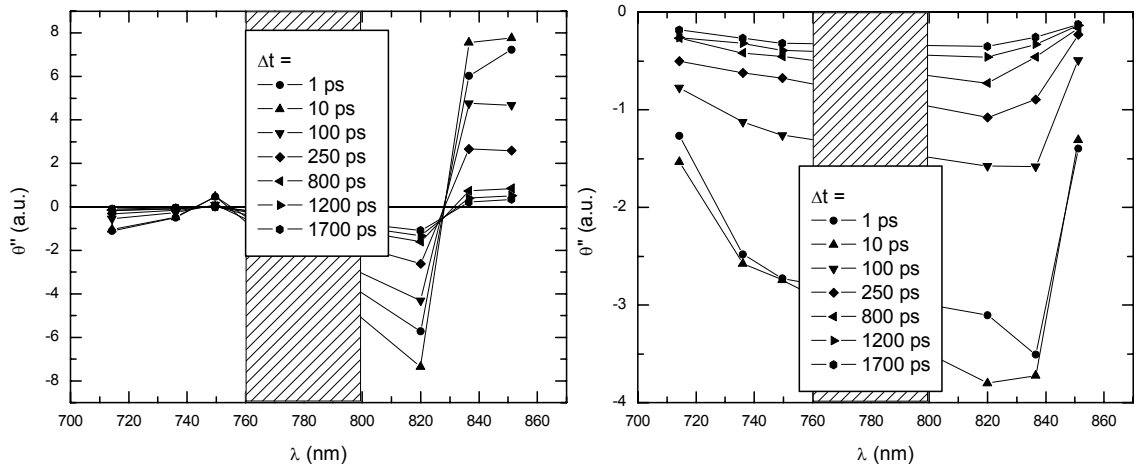

Figure 5.2: Rotation θ' (left) and ellipticity θ'' (right) at several pump-probe delay times.

Now, a sum of two exponential decays is needed to make an adequate fit of the data:

$$\theta = a_1 \exp\left(-\Delta t / \tau_1\right) + a_2 \exp\left(-\Delta t / \tau_2\right) \tag{5.1}$$

with amplitudes $a_{1(2)}$ and time constants $\tau_{1(2)}$. The fitting parameters are presented in figure **5.3**, while in figure **5.4** the quality of some fits can be compared to the raw data.

As already mentioned in section 4.2, the longest time constant of the two is considered to correspond to the electron spin relaxation time. The shorter one could be a combination of the effects of recombination, diffusion and an enhanced spin relaxation rate. This constant ranges from 20 to 150 ps, while a spin relaxation time of 150 up to 3000 ps has been observed. The amplitudes for the two decays are dependent on wavelength as well. in order to show their quality.

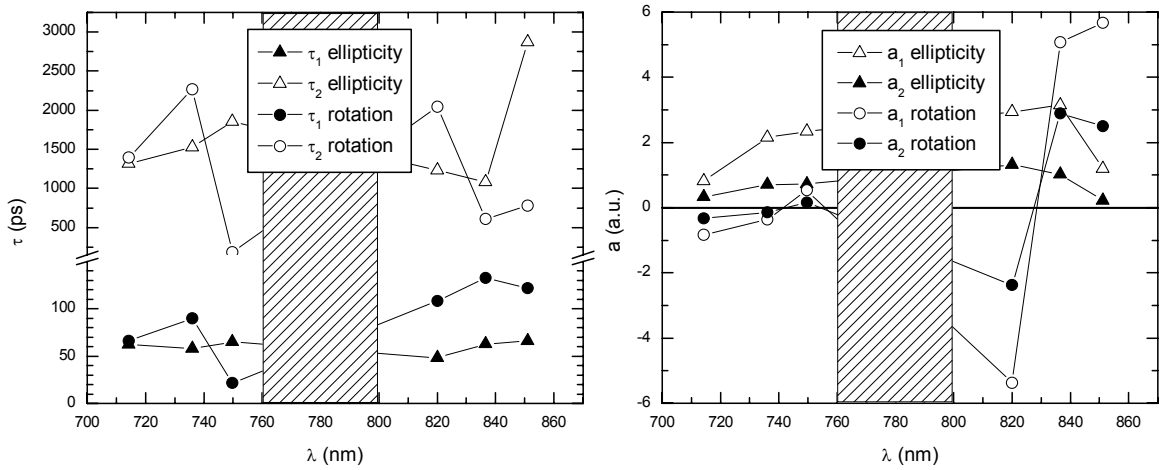

Figure 5.3: Time constants and signal amplitudes for ellipticity and rotation signal from double exponential fits of TiMMS timescans. The shaded area indicates the notch filter range.

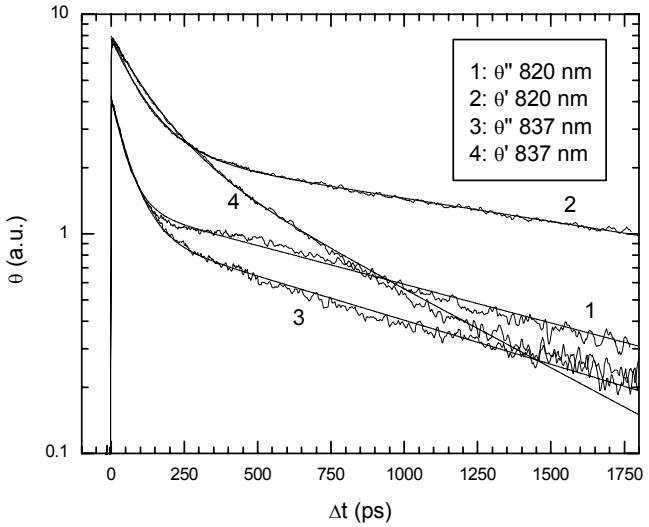

Figure 5.4: Combined plots of the double exponential fits compared to their data for rotation θ' and ellipticity θ'' for a probe wavelength of 820 nm and 837 nm.

Because during experiments nothing is changed for the pump beam, the spin dynamics in the sample should be identical for every measurement. Nonetheless, the results show strong variations in amplitude as well as decay times. Therefore, numerical simulations have been done to make clear exactly what parameters influence the Kerr effect.

5.2 Calculation of Kerr effect

A model has been set up to calculate the Kerr response for the spin channel of the all-electrical spin injection and detection device. This model couples a *z*-dependent complex magneto-optical constant *Q*

to the rotation θ' and ellipticity θ'' in the reflection of linearly polarised light, incident perpendicular to the surface. Therefore, the following relation is constructed:

$$\theta' + \mathrm{i}\,\theta'' = \int_0^\infty f_\lambda(z)\,Q(z)\,dz \tag{5.2}$$

using a complex relational function $f_\lambda(z)$ that is calculated numerically (results are shown in figure **5.6**). This relation is demonstrated to be valid for sufficiently small Q: $|Q| \le 0.01$.

For the computation of $f_\lambda(z)$ the multilayer matrices introduced in section 2.4 are used. The function is only determined for the GaAs layers in the base heterostructure of the all-electrical spin injection device: 200 nm *n*-GaAs on 200 nm $Al_{0.3}Ga_{0.7}As$ on 0.5 mm *i*-GaAs. First, each GaAs layer is divided into thinner layers (see figure **5.5**). The medium boundary matrices and medium propagation matrices are calculated, using a random value for Q in each layer. Then the Kerr effect is determined, while varying Q for a specific layer at depth z. The proportionality of the difference in the Kerr effect to the variation of Q in that layer is the value of $f_\lambda(z)$. The result is empirically determined to be independent on the Q-values of the other layers while testing a specific layer, as long as the condition $|Q| \le 0.01$ is fulfilled.

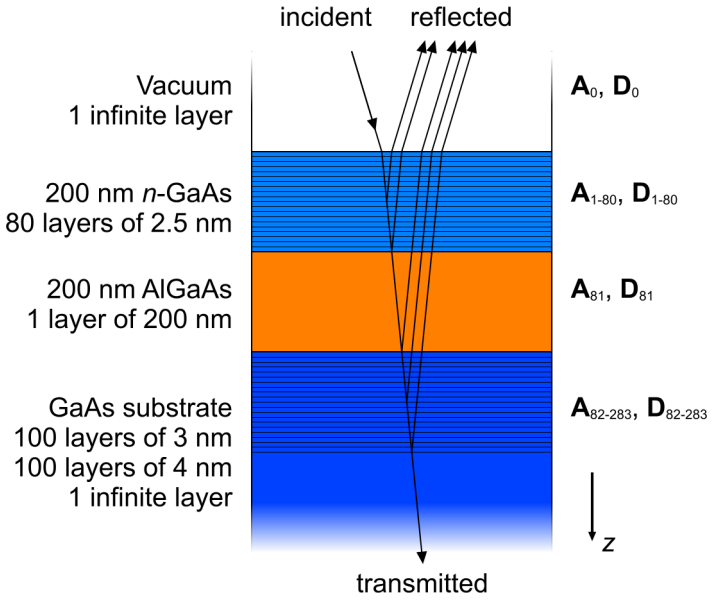

Figure 5.5: Arrangement of layers with which $f_\lambda(z)$ is determined.

The function $f_\lambda(z)$ is determined up to 700 nm into the substrate, for probe wavelengths of 700 nm to 850 nm and perpendicular incidence of probe light. The direction of Q is in the z-direction as well. Literature values have been used for the refractive index n for GaAs[11] and AlGaAs[22] at a temperature of 300 K, corrected with the temperature coefficient in [11] to values for 5 K. The absorption coefficient for GaAs fluctuates strongly around the band gap. This is accounted for, using values from [23] for intrinsic GaAs to describe both the transport channel and the substrate. The deviation caused by the *n*-doping of $5 \cdot 10^{16}$ cm^{-3} is supposed to be negligible.

Only for the spin transport channel and the substrate has $f_\lambda(z)$ been determined, because optical injection into $Al_{0.3}Ga_{0.7}As$ with its higher band gap is not possible with a pump wavelength of 780 nm. The results for both the real and the imaginary part of $f_\lambda(z)$ are plotted for a selection of wavelengths in figure **5.6**.

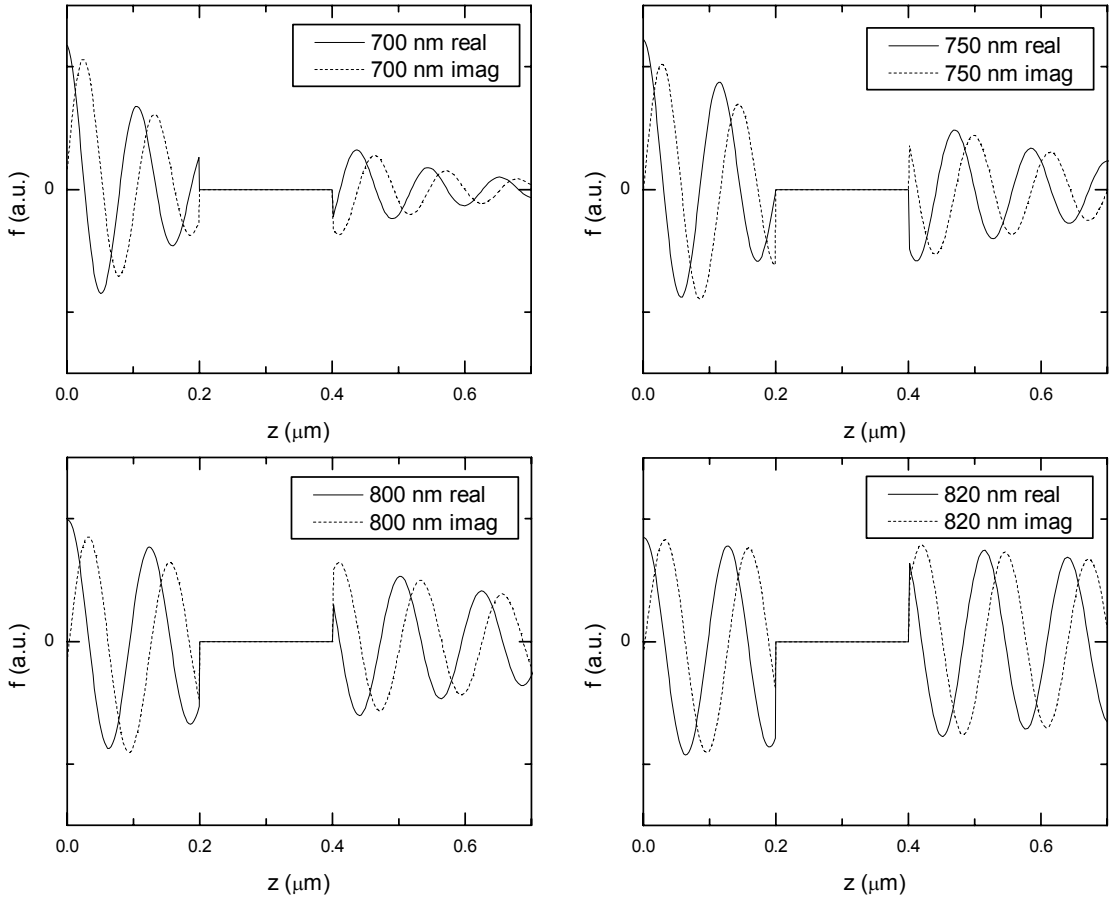

Figure 5.6: Dependence of the Kerr rotation on the magneto-optical constant via the real (a) and imaginary (b) part of $f(z)$ for selected wavelengths.

The three parts of the sample can be recognised by the transitions at 200 and 400 nm. Some properties of the relational function are easily understood. The periodic behaviour, with the real and imaginary parts shifted in phase 90 degrees, originates in the wave-like nature of light. The periods have a size half the wavelength of the probe laser pulses inside the material: $\lambda/2n$. This is because the electromagnetic wave on which Q produces an effect has to travel forth and back from the surface of the sample, advancing its phase with $\exp(\mathrm{i}nz/\lambda)$. Furthermore, exponential damping by absorption can be seen, being dependent on the photon energy via the absorption coefficient. However, the added value of the matrix method used to determine the relational function is clearly visible when plotting the absolute value $|f_\lambda(z)|$ as in figure **5.7**. The ripples seen in the spin transport channel are attributed to reflections at the GaAs / AlGaAs interface.

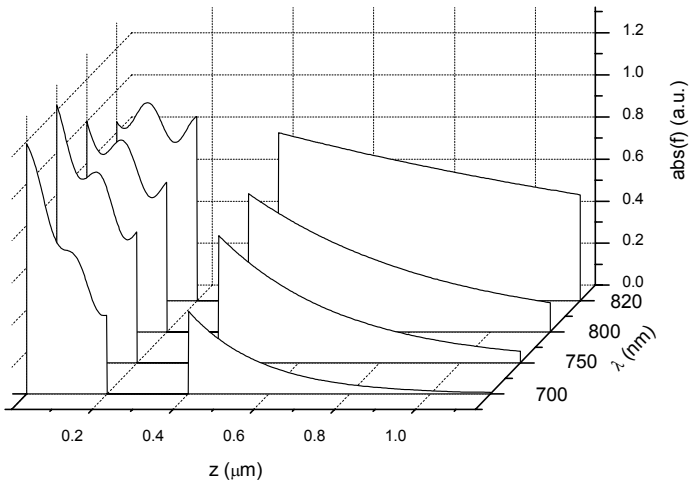

Figure 5.7: Absolute value of f_λ for selected wavelengths.

The situation investigated here deviates from more common situations where the Kerr effect is determined for layers thin or thick compared to the optical path length. Following the relation (5.2), the final Kerr effect is found by integrating the relational function multiplied with $Q(z)$. The positive and negative contributions of $f_\lambda(z)$ in the spin transport channel add up to a value very sensitive to the chosen wavelength.

In situations where the investigated layer is much thinner than the probing wavelength, the contribution of $f_\lambda(z)$ would be purely positive. This is also the case when the optical path length is shorter than the wavelength. On the other hand, in situations where the layer is much thicker than the path length, each negative contribution is smaller than its preceding positive contribution, resulting in a wavelength-insensitive result as well.

5.3 Magneto-optical constant Q

To apply the function calculated in the previous section, the magneto-optical constant $Q(z)$ must be determined throughout the sample. First, the Kerr effect will be determined for a homogeneous Q in the spin transport channel and $Q = 0$ for $z > 200$ nm. For this situation, equation (5.2) can be rewritten as:

$$\theta' + \mathrm{i}\theta'' = Q\int_0^d f_\lambda(z)\,dz = QF_\lambda \tag{5.3}$$

with F_λ the integral of f_λ over the spin transport channel, $0 < z < 200$ nm. The real and imaginary parts of F_λ are shown in figure **5.8** as a function of wavelength.

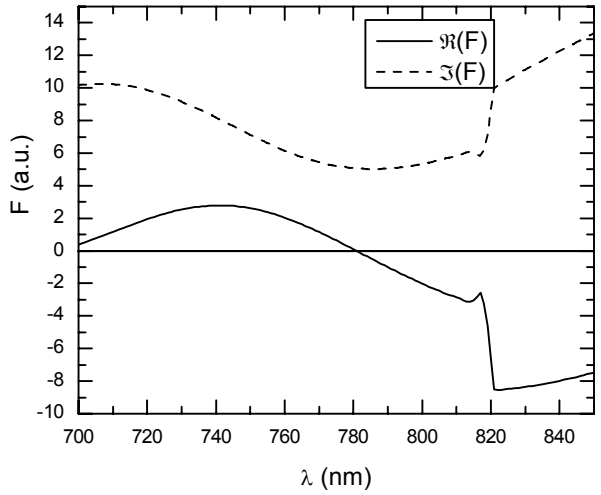

Figure 5.8: Real and imaginary parts of F_λ as a function of wavelength.

The next step is to estimate Q as a function of wavelength. As mentioned in section 2.4, it will show a Kramers-Krönig relation between the imaginary and real part. In section 4.1 is explained that the probe pulse bandwidth can be used to determine the width of the resonance peak. Therefore, the shape shown in figure 5.9 has been used to simulate the Kerr effect for a probe bandwidth of 8 nm.

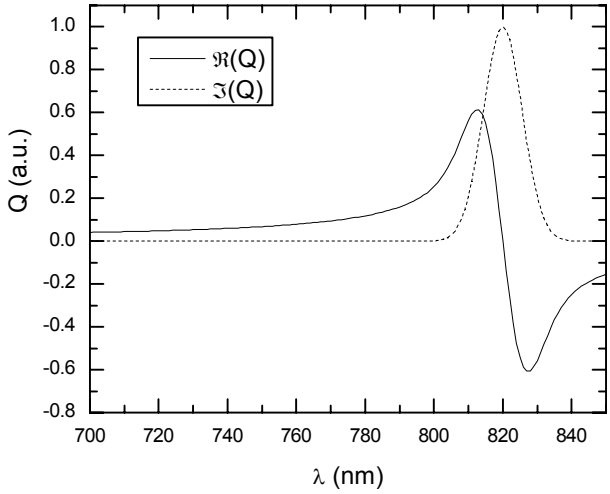

Figure 5.9: The imaginary and real parts of Q as a function of wavelength, related via Kramers-Krönig.

The Kerr rotation θ' and ellipticity θ'' can now be calculated using equation (5.3):

$$\theta' = \Re(F_\lambda)\Re(Q) - \Im(F_\lambda)\Im(Q) \text{ and} \tag{5.4}$$

$$\theta'' = \Re(F_\lambda)\Im(Q) + \Im(F_\lambda)\Re(Q). \tag{5.5}$$

The results are shown in figure **5.10**.

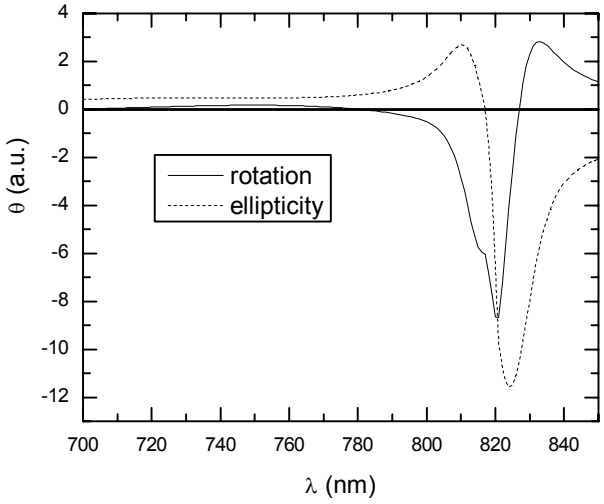

Figure 5.10: The imaginary and real parts of Q as a function of wavelength, related via Kramers-Krönig.

The calculation is compared with the amplitudes a_2 of rotation and ellipticity retrieved from the two-colour TiMMS timescans, presented before as open triangles and circles in figure **5.3**. These represent the spin density of the conduction electrons past recombination.

Clearly there is a correspondence between the simulations and the measurements. Comparing the values for rotation, the spin signal shows a gradual increase from 700 to 750 nm, then peaking down at 820 nm and suddenly changing sign to a positive maximum between 830 and 840 nm. As for ellipticity, the gradual growth from 700 up to 800 nm is comparable, although the sudden sign change in the simulation result at 815 nm cannot be seen in the measurements.

A refinement of the wavelength dependency of Q might further improve the correlation between measurement and simulation, taking into account the inhomogeneous distribution of carriers in the transport channel. When the carrier density increases, the density of states will be filled up to a higher energy, causing the resonance peak of the imaginary part of Q to shift to higher energies. Furthermore, the contribution of spin polarisation to the magneto-optical constant will be increased by the higher conduction band electron density. The alternating positive and negative effects in $f_\lambda(z)$ should thus be weighted by carrier concentrations as shown in figure **3.4**.

However, the origin of the time constant variations in the two-colour TiMMS timescans are not explained by the simulations. These can be attributed to non-linear effects, the magneto-optical constant not being linearly proportional to the spin polarisation. Another possibility is that spin injected in the substrate plays a role and that the measurements are a mix of the spin transport layer and the intrinsic substrate. If the electron spin relaxation in the substrate has a time constant comparable to that in the top layer, it would be difficult to distinguish between the two.

5.4 Conclusions

In this chapter, simulations give insight in the construction of the magneto-optic Kerr effect in a non-trivial sample. It shows that the choice for the wavelength when probing a sample is important, and the

simulations can help making the decision. The results for the calculations agree with the measurements to a certain extent. After a refinement of some parameters, this method could be a powerful way to be able to retrieve spin information from specific depths in non-homogeneous samples. Further measurements with samples specially prepared for this goal can help with refining. For example a wedge of 0 to 1000 nm GaAs on AlGaAs might confirm the periodicity of $f_\lambda(z)$, while a more homogeneous electron distribution can eliminate some uncertainties in Q and F_λ could be directly measured.

6 Spin transport

As described in chapter 3, the all-electrical spin injection and detection device is based on its long spin lifetime and spin injection and detection by tunnel barriers. Other spin-related parameters that need to be controlled when engineering the device are the spin diffusion and spin mobility constants in the spin transport channel. After spin is injected, it is subject to these parameters while being transported from one electrode to the other. Therefore, spin diffusion and drift are measured optically in this chapter. They are determined by monitoring a spin package, both temporally and spatially, after it is injected optically. While diffusion dilutes the package spatially, an electric field cause it to be displaced. Measurements are done using TiMMS timescans with the probe spot moving independently from the pump spot. The results are compared with calculations and numerical simulations.

6.1 Spin diffusion

When spin is injected in the channel optically, it will be subject to the spin dynamics described in section 2.3. In this section, the effects of spin diffusion and spin relaxation are accounted for, resulting in the following differential equation for the spin density $n_\uparrow - n_\downarrow$:

$$\frac{\partial}{\partial t}\left(n_\uparrow - n_\downarrow\right) = D_s \nabla^2 \left(n_\uparrow - n_\downarrow\right) - \frac{\left(n_\uparrow - n_\downarrow\right)}{\tau_s} \tag{6.1}$$

where D_s is the spin diffusion constant and τ_s the spin relaxation constant. The separate elements have already been discussed in chapter 2. In the experiments, the spatial laser intensity profile is Gaussian, resulting in a spin density spot that is Gaussian as well directly after optical injection. Therefore, the spot at delay time $\Delta t = 0$ is described as:

$$\left(n_\uparrow - n_\downarrow\right)\left(\mathbf{x}, t = 0\right) = A_0 \exp\left(-\frac{\left|\mathbf{x} - \mathbf{x}_0\right|^2}{w^2} \right) \tag{6.2}$$

with $\mathbf{x}_0$ the location of the spot's centre, A_0 the amplitude and w the width of the spot. For this initial value problem the differential equation (6.1) can be solved easily. The result can be written as:

$$\left(n_\uparrow - n_\downarrow\right)\left(x, t\right) = \frac{A\left(t\right)}{w\left(t\right)^N} \exp\left(-\frac{\left|\mathbf{x} - \mathbf{x}_0\right|^2}{w\left(t\right)^2} \right) \tag{6.3}$$

where the amplitude A and width w are now functions of time. The power N is the dimension of the spot. In the case of optical spin injection where diffusion in the z-direction is ignored, the dimension will be $N = 2$.

The amplitude and width are described with the following functions of time:

$$A(t) = A_0 \exp\left(-\frac{t}{\tau_s}\right) \tag{6.4}$$

$$w(t) = \sqrt{4D_s(t + t_0)} \tag{6.5}$$

where t_0 defines the width of the spot at $t = 0$. This result is visualised in figure **6.1** for $N = 1$ and dimensionless parameters $D_s = 1$, $\tau = 1$ and $w(t = 0) = 1$.

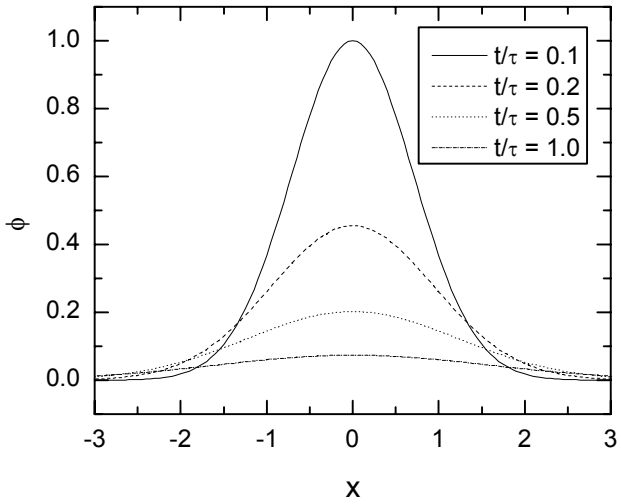

Figure 6.1: Gaussian profile subject to diffusion and relaxation.

The influence of diffusion can be seen by the increase of spin density at $x = 2$, while the area under the curve decreases by relaxation. When such a profile is measured for an optically injected spin package, the spin diffusion constant can thus be retrieved by determining the width of the Gaussian spin density profile as a function of time. Using equation(6.5), the spin diffusion constant is then defined as

$$D_s = \frac{1}{4}\frac{\partial}{\partial t} w^2 . \tag{6.6}$$

Probing the spin package spatially is done by independently moving the probe spot on the sample from the pump spot by changing the angle at which the probe spot enters the objective in front of the sample, separating them with a distance Δx (see figure **6.2**). The probe beam width, passing the centre of the objective, is chosen to be wider than the pump probe beam, entering the objective at the side. Therefore, the probe spot on the sample will be smaller than that of the pump. The pump spot will be elliptical because of asymmetrical refraction by the objective.

For the diffusion measurements that follow here for the spin transport channel, pump and probe with different colours are used, i.e. they have a wavelength of respectively 785 ± 8 nm and 807 ± 8. The probe, with a time averaged intensity of 0.60 mW, is focused to a spot of 3 μm diameter, while the pump with a time averaged intensity of 0.22 mW creates spin package with a diameter of 8 μm. The sample is cooled to a temperature of 5 K.

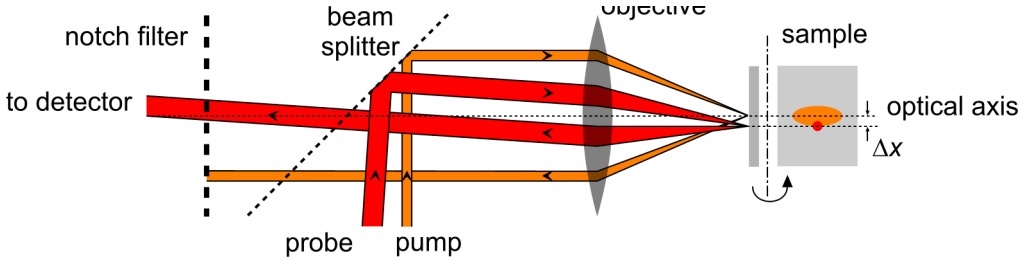

Figure 6.2: Schematic illustration of the movement of the probe spot on the sample by changing the angle at which the probe beam enters the objective. On the right, a top view of the sample is shown with the spot separation Δx.

To get a spin profile as a function of time, TiMMS timescans have been obtained using the rotation of the probe reflection with different pump-probe spot distances Δx. The resulting scans are combined to time-resolved spatial spin density profiles, one constructed for each delay time. Two timescans at different pump-probe distances $\Delta x = 9.0$ µm and $\Delta x = -4.2$µm obviously show the effect of diffusion in the left plot of figure **6.3**. While the former is gradually increasing, the latter rapidly decreases. In the right plot of figure **6.3**, spin density profiles are showed for a selection of delay times. The pump-probe separation for which the timescans are shown is indicated by the two vertical lines Note that this profile is actually the convolution of two profiles, that of the spin and that of the probe.

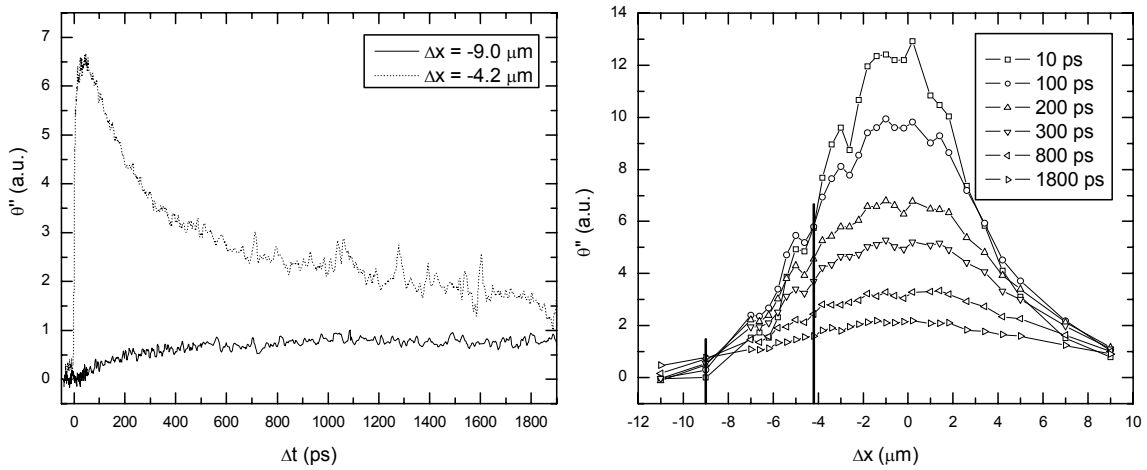

Figure 6.3: Timescans at two different pump-probe separations Δx (left) and spin profiles at a selection of delay times (right).

A broadening can be seen in the spin density profiles by a decrease of intensity in the centre while at the edge the intensity increases slightly. To determine the spin diffusion constant D_s from these measurements, for each delay time a Gaussian has been fitted. The square width w^2 of the profiles is then plotted as a function of time in figure **6.4**, its slope determining the diffusion via (6.6). Two regions have been indicated with a linear fit. Because the convolution of two Gaussians with width $w_{1(2)}$ results in a combined width $w^2 = w_1^2 + w_2^2$, the width of the probe spot acts purely as an offset, not influencing the actual slope of the curve. In the figure, the 95% confidence margins of the fits are plotted as well.

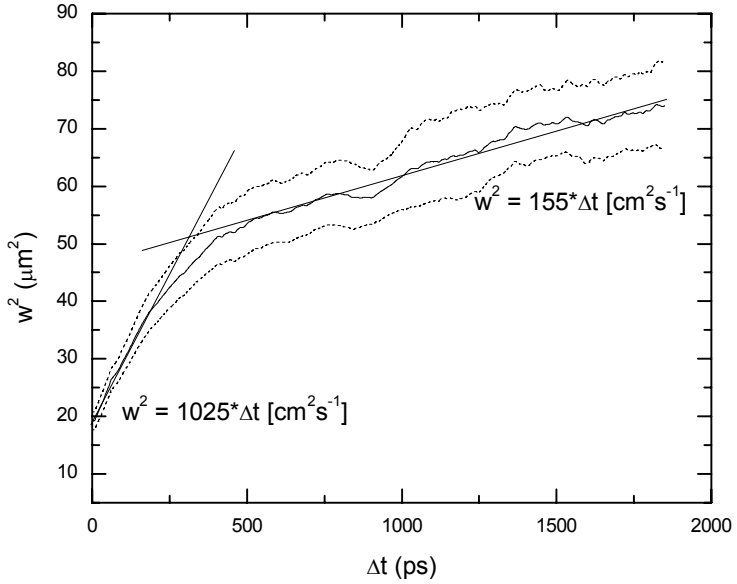

Figure 6.4: Width w^2 of a Gaussian spin package as a function of time. The solid line is the best fit, while the dashed lines are the 95% confidence margins.

The slope is not constant, indicating that the diffusion constant changes in time. In the first 250 ps it is remarkably higher at 256 cm^2s^{-1} than in the second part after 500 ps, where it's only 39 cm^2s^{-1}.

To retrieve additional information on the size of the spin package at a longer timescale, a scan at a *negative* delay time has been done, where the remainder of the previous pump pulse can be seen, 12.5 ns earlier at a pump frequency of 80 MHz. Because the signal at this delay time is very weak compared to the noise and to suppress a possible offset in the signal, a magnetic field sweep has been done for each pump-probe separation Δx. An in-plane magnetic field has been used to let the spin precess. The Larmor frequency at which the spin rotates from up to down and back is proportional to the magnetic field. When probing at a fixed delay time, the amplitude will show oscillations. This is shown in figure **6.5** at a delay time of -100 ps, corresponding to 12.4 ns relative to the preceding pump pulse. A cosine is fitted through the data, for which the amplitude determines the spin density.

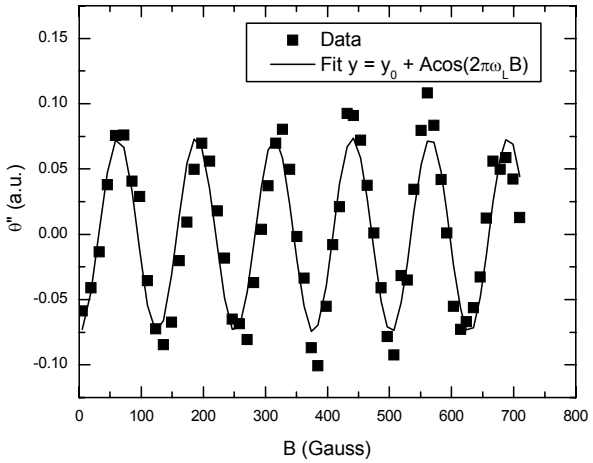

Figure 6.5: Oscillations by Larmor precession in a field sweep at a negative delay time of Δt = -100 ps.

In figure **6.6**, the amplitudes of the field sweeps at different pump-probe distances Δx are combined to a profile at 12.4 ns. Fitting the data points yields a square width of w^2 = 300 µm. When adding this value as an imaginary point at Δt = 12400 ps in figure **6.4**, the diffusion constant at the longer time-scale is refined to a value of $D_s = 45 \pm 10$ cm^{2}s^{-1}.

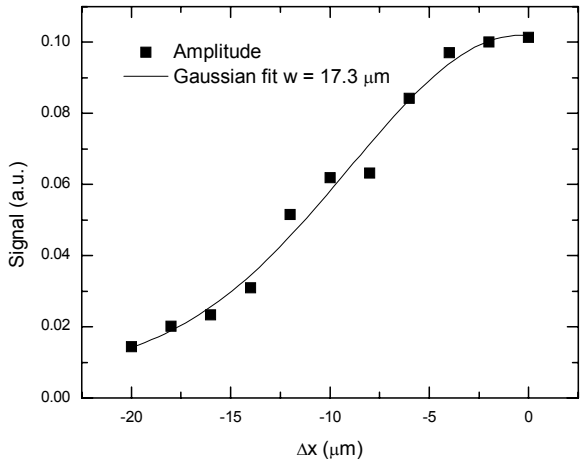

Figure 6.6: Amplitude of field sweeps at Δt = 12.4 ns with Gaussian fit.

The transition in diffusion constant around 400 ps is remarkable. The time scale at which the higher diffusion rate takes place coincides roughly with the carrier lifetime in the sample. An explanation for this is sought in the non-linearity of spin dependent electron-hole recombination, visualised in figure **6.7**. The recombination rate is determined by the electron density multiplied with the hole density. Both electrons with spin up and spin down will recombine, but when the spin up carrier concentration is significantly larger than the spin down density, i.e. when the excitation density is of the order of magnitude of the equilibrium carrier concentration or larger, more spin up electrons than spin down electrons will recombine. Therefore, the spin density $n_\uparrow - n_\downarrow$ will decrease. This effect is largest at the centre of the spin package, while at the tail the difference in spin up and spin down density is so low

that the effect is negligible. The result is a spin package that seems to be broader after recombination compared to its initial width. In fact, its profile is not true Gaussian anymore. Fitting it anyway will result in a fit with increasing width. Excitation density plays an important role here, thus this effect is supposed to be larger when higher pump power is used.

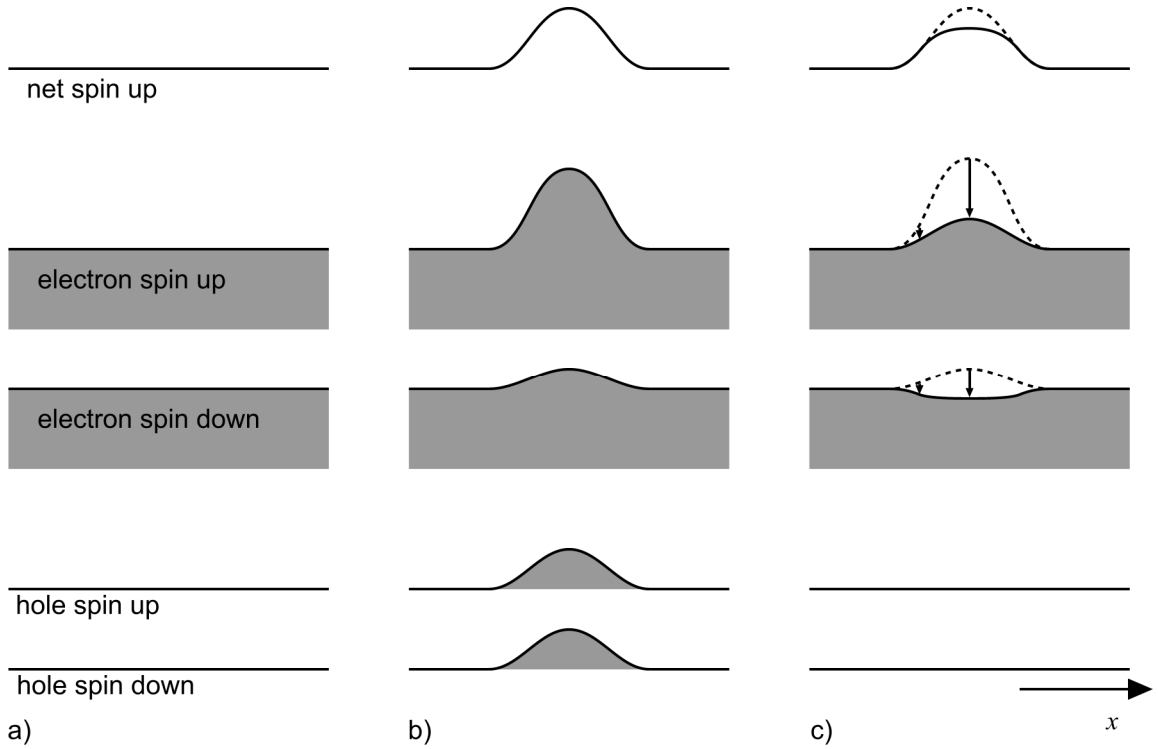

Figure 6.7: Influence of recombination on spin density. When in a neutral band (a) a spin package is optically injected (b), the spin up electrons at the peak in the conduction band recombine at a higher rate than the spin down electrons, resulting in a broader spin package (c).

To explain the increased diffusion rate at delay time $\Delta t < 250$ ps in figure **6.4**, this theoretical effect must play a significant role, exceeding the true diffusion process. Besides, in section 2.3 is mentioned that in the presence of holes the spin diffusion rate can be an order of magnitude lower than without holes, because of the lower hole diffusion constant and the Coulomb interaction between electrons and holes. Therefore, a simulation has been run to quantify this effect.

The recombination of a spin package in the conduction band is simulated for an equilibrium electron density of $5 \cdot 10^{16}$ cm^{-3}. The exciton density used is $5 \cdot 10^{17}$ cm^{-3}. As initial condition, the injected spin up to spin down ratio is 3:1, following the optical selection rules as explained in section 2.2, while the holes are neutrally polarised due to the fast hole relaxation rate. The initial width is 5 μm and the carrier lifetime is set to 100 ps. Diffusion is switched off for the moment, so that the effect of pure recombination is retrieved. The following differential equation is used to calculate the recombination rate:

$$\frac{\partial}{\partial t} n_{\uparrow(\downarrow)} = -\frac{n_{\uparrow(\downarrow)} p}{n_0 \tau_r} \tag{6.7}$$

where p is the hole density, n_0 the equilibrium electron density and τ_r the carrier lifetime. Because of the fast hole spin relaxation, no distinction is made between spin up and spin down holes.

Figure **6.8** shows the result of the simulation. The spin up and spin down conduction band profiles are showed for a selection of times after optical injection on the left, while the accompanying spin density $n_\uparrow - n_\downarrow$ is displayed on the right. The resulting spin profiles become visibly flatter in the centre, resulting in a broader spin package although there is no real spin diffusion simulated.

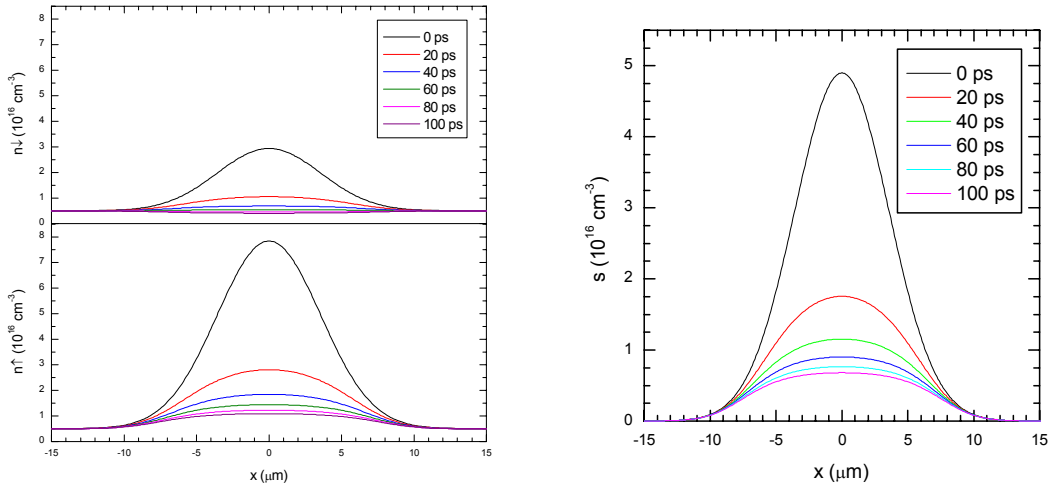

Figure 6.8: Snapshots of the spin up and spin down electron density profiles subject to asymmetrical recombination at several time intervals after optical injection.

The profiles are fitted with Gaussians to measure their width as a function of time. Results are shown in figure **6.9**, together with 95% confidence boundaries and $\frac{\partial}{\partial t} w^2$ to compare the effect to the measurements.

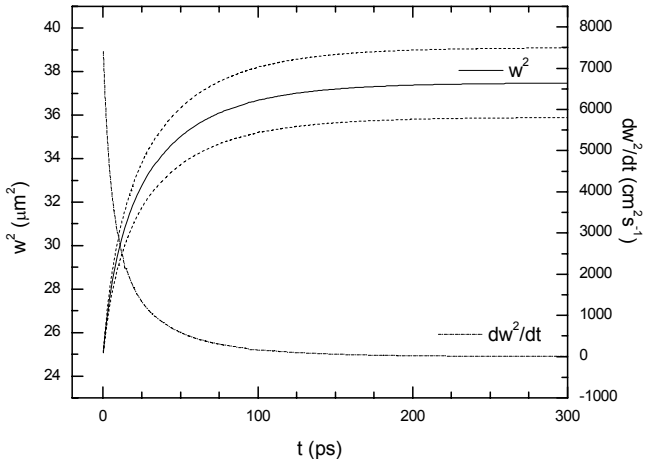

Figure 6.9: Simulation of influence of non-linear recombination on the width of a spin package. The solid line surrounded by the dashed 95% confidence bounds shows the width of the package, while the dot-dashed line shows the derivative.

These results show that for a reliable determination of spin diffusion with the optical means described here, one should focus at the diffusion constant after electrons and holes have recombined. Before, the spin dynamics are believed to be mainly dominated by recombination, while diffusion of spin polarised electrons is hindered by the presence of slower holes. Moreover, when injecting electrically instead of optically, holes are not present. The value of $D_s = 45 \pm 10$ cm^{2}s^{-1} at a temperature of 5 K can thus be used as the spin diffusion constant for the spin transport channel. By comparison, the electron diffusion constant for GaAs is reported to be up to 200 cm^{2}s^{-1} [11].

6.2 Spin drift

Another important process for the all-electrical spin injection and detection device is spin drift in an electrical field. To investigate the behaviour of a spin package in the spin transport channel when a voltage is applied, experiments similar to the above spin diffusion measurements have been carried out. An in-plane electron current is created using two ohmic contacts, while spin is injected optically. The situation is shown in figure **6.10**, indicating the location at which drift is being measured. To ensure there is no optical interaction with the structures grown on the channel, a location outside the active channel is chosen in a symmetrical situation between two ohmic contacts. Note that in the figure, the square gold pads are isolated from the channel. The arrows show how electrons flow from one to the other electrode, creating a homogeneous current at pump location. An applied voltage of 5 V leads to a current of 5 mA at a temperature of 5 K. Single colour timescans are obtained at a wavelength of 813 ± 7 nm. The pump intensity is set at 1.0 mW, the probe at 0.4 mW.

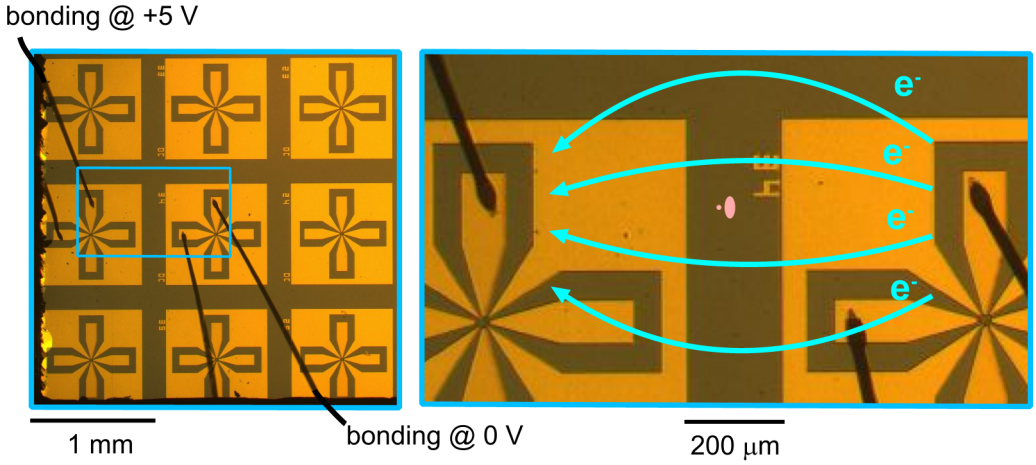

Figure 6.10: Top view of the sample and the location where drift measurements have been carried out. The ohmic contacts are indicated with the bondings, while the pump and probe spots are shown on the right. The arrows are an indication for the current distribution.

For a certain pump-probe distance Δx, two TiMMS timescans are made successively, one with and one without current. Then Δx is altered, repeating the two measurements et cetera, until the complete spin packages have been visualised. This way, the profiles with current and without current are measured

simultaneously, ensuring that any consistent difference is caused by the current. Like in the diffusion experiments, the spin profiles that are obtained are fitted with Gaussians as a function of time. The parameter of interest is now x_0 though, the centre of the spin package. The difference Δx_0 between the centres with field and without field is plotted in figure **6.11**.

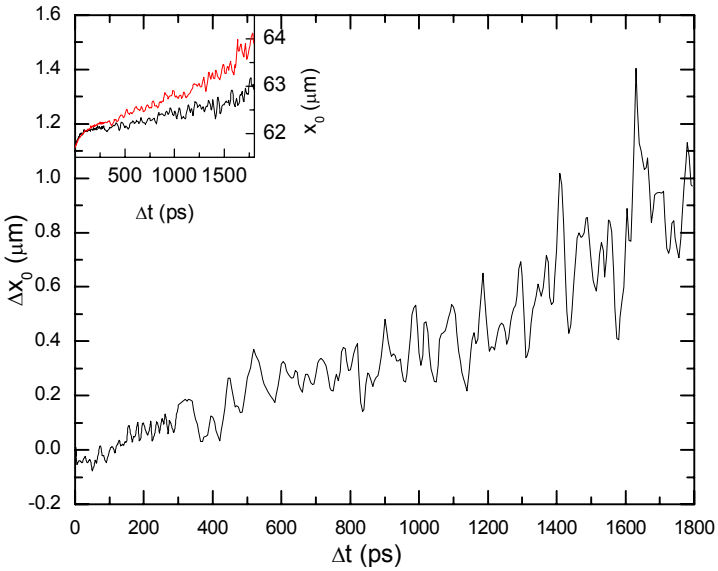

Figure 6.11: The movement of the centre of the spin package as a function of time by a current of 5 mA.

Note that the inset in figure **6.11** shows a displacement of both spin packages. This emphasises the need to perform measurements for both situations, with and without field. The shift of x_0 without field is devoted to optics. The delay line moves over 30 cm to create a delay time of 1800 ps. When not perfectly aligned, the probe beam can shifts its path slightly.

The relative movement of the spin package can be clearly seen. It has been displaced by 0.9 ± 0.2 µm over 1800 ps, resulting in an average speed of $55 \cdot 10^3$ cms^{-1}. By comparison, the average electron speed is calculated using the current magnitude I, channel width L, channel depth D and carrier concentration n as follows:

$$\tilde{v} = \frac{I}{neA} \tag{6.8}$$

where e is the charge of the electron and $A = LD$ is the area through which the current is spread. The assumption is made that the current is equally distributed over a width of $L = 1$ mm at the location of the drift measurement. The depth of the channel is $D = 200$ nm and the electron concentration is defined by the doping of $n = 5 \cdot 10^{16}$ cm^{-3}. The average speed of the electrons is thus calculated to be $313 \cdot 10^3$ cms^{-1} while the distance covered in 1800 ps should then be 5.6 µm. The deviation of this calculated value with the speed measured optically can be contributed to either a wrong estimation of the current density, or to a discrepancy in spin mobility and electron mobility.

Comparing the spin speed of $55 \cdot 10^3$ cms^{-1} to the electric field of 5 V over 1 mm results in a spin mobility of $(1.1 \pm 0.3) \cdot 10^3$ cm^{2}V^{-1} s^{-1}. This has the same order of magnitude as literature values, be it on the low side[11].

6.3 Conclusions

Visualising diffusion and drift of an optically injected Gaussian spin package can be done effectively by monitoring its profile as a function of time. In an electric field it has been seen displaced over a micrometer. For the spin transport channel, the mobility has been determined to a value of $(1.1 \pm 0.3)\cdot 10^3$ cm^2V^{-1} s^-1. By measuring the broadening of the package in time, the spin diffusion constant is determined as 45 ± 10 cm^2s^{-1}. These values are of the same order of magnitude as electron mobility and drift for *n*-GaAs at these temperatures, be it somewhat smaller.

Before electrons and holes are recombined, improved diffusion appears to have been observed. A simulation of recombination using separate spin up and spin down electron bands can explain this behaviour, which originates in asymmetrical spin up and spin down recombination at the centre of the spin package. It turns out that in the presence of holes, diffusion is more difficult to measure. Additional research could be performed for setting up a complete spin recombination and diffusion model, varying several parameters for experiments and model.

When the sample would have a much longer relaxation time, orders of magnitude larger than the recombination time, the signal at longer pump-probe delay times is increased. This would facilitate the accuracy of the measurement technique described.

7 Optical detection of electrical injection

An all-electrical spin injection and detection device consists of several elements that require working together well in order to achieve magnetoresistance. In this chapter, an attempt is made to optically detect electrically injected spin, in order to prove that the electrical injection electrode functions properly and to determine its efficiency. Therefore an experimental setup is described, after which simulations are performed to determine the signal that can be expected. Then measurements are reported, followed by a discussion on the all-electrical functionality of the device.

7.1 Setup description

In this section a technique is described to optically detect electrically injected spins. Using this technique a spin polarised current into the transport channel can be visualised using the magneto-optic Kerr effect. Only recently, this combination of injection and detection has resulted in images of electrically injected spin transport[20].

The ferromagnetic electrodes of the all-electrical spin injection and detection device are magnetised in plane in the *y*-direction, as mentioned in chapter 3. This defines the orientation of the electrically injected spins to be in-plane as well, while the magneto-optic Kerr effect is most sensitive to out-of-plane spin. Therefore, electrically injected spin is hard to be detected directly using this optical detection method. An in-plane magnetic field, perpendicular to the electrode magnetisation, is used to create a torque on the spin polarised electrons so that they precess out-of-plane obeying (2.10). The precession of a direct spin polarised current is visualised in figure **7.1**.

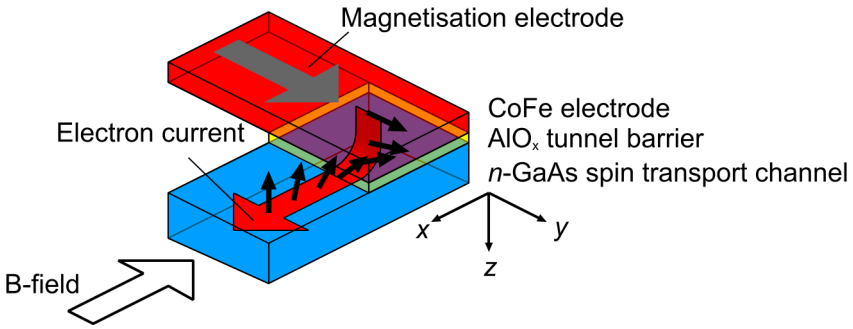

Figure 7.1: Spin precession in a magnetic field after electrical injection.

For optical detection of the spin polarised electrons in the spin transport channel, the TiMMS setup is adjusted to the setup shown in figure **7.2**. A Ti:sapphire pulsed laser is used as source for the probe

beam. The probe is linearly polarised at 90° and is modulated by a PEM set at 45° at a frequency f_{PEM}. The alternately left and right polarised probe is then focused on the sample near the spin injection electrodes. Because the magneto-optic Kerr effect originates in the difference in reflection for these two optical modes, the intensity variation of the reflected laser beam is a measure for spin density at the laser spot on the sample. An optical detector measures the reflection and a lock-in amplifier is used to amplify the spin signal.

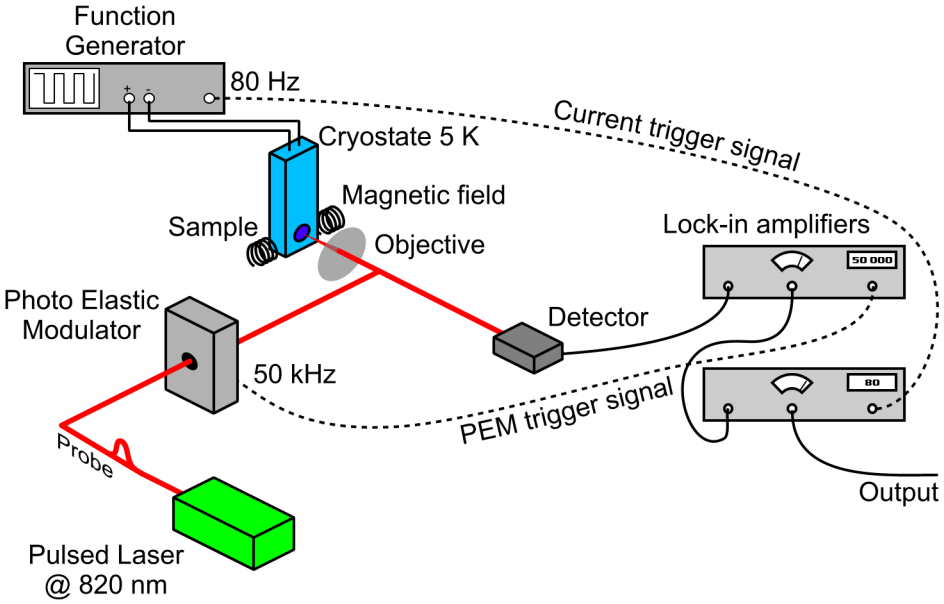

Figure 7.2: Setup for optical detection of electrically injected spin.

To electrically inject spin, a function generator is used to induce an alternating current through a tunnel barrier at a frequency $f_{inject} << f_{PEM}$, using one ferromagnetic electrode and one ohmic contact of the device shown in figure **3.3**. A spin polarised current, quantised in the y-direction, tunnels into or out of the spin transport channel. An adjustable magnetic field in the x-direction creates an out-of-plane component. A second lock-in amplifier is placed after the first, locked to f_{inject}. This modulation ensures that any measured signal is caused by the current.

7.2 Precession

To determine the magnitude of the magnetic field needed to efficiently measure out-of-plane spin near the injection electrode, the same model as in [20] is used. It incorporates spin diffusion and drift in one dimension, spin precession and spin relaxation for continuously injected in-plane spin under an electrode. With this model, the z-component of spin S_z is defined as a function of magnetic field B_x and distance x from the injection electrode:

$$\frac{S_z(B_x,x)}{S_0} = \int_x^{x+W}\int_0^{\infty} \frac{1}{\sqrt{4\pi D_s t}} e^{-t/\tau_d}\, e^{-(x'-v_d t)^2/4D_s t} \sin(\omega_L t)\, dt dx' \qquad (7.1)$$

where S_0 is the spin density directly after injection in the y-direction. Furthermore, W is the width of the electrode, τ_s is the spin lifetime, D_s the spin diffusion constant, v_d the drift velocity and ω_L the Larmor precession frequency, proportional to the magnetic field and the gyromagnetic ratio via (2.10).

All these parameters have already been determined before or are estimated here. For the all-electrical injection and detection device, $D_s = 45$ cm^{2}s^{-1}, $\tau_s = 1500$ ps, $\gamma = 6.7 \cdot 10^9$ T^{-1}s^{-1} and $W = 250$ nm. At a typical voltage of 150 mV over the tunnel barrier, suitable for electrical spin injection, a current of 2 μA is induced. Distributing this current over the channel with a width of approximately 3 μm, a depth of 200 nm and an electron concentration of $5 \cdot 10^{16}$ cm^{-3} results in an average drift velocity of $4.2 \cdot 10^4$ cms^{-1}. Using these values, the profiles shown in the left plot of figure **7.3** have been calculated, determining $S_z(x)$ for different values of B_x. The convolutions of these curves with a Gaussian laser profile having a width of $w = 2.5$ μm are shown on the right as well. The spin under the electrode, located at $|x| \leq 0.125$ μm, has been ignored when calculating the convolutions.

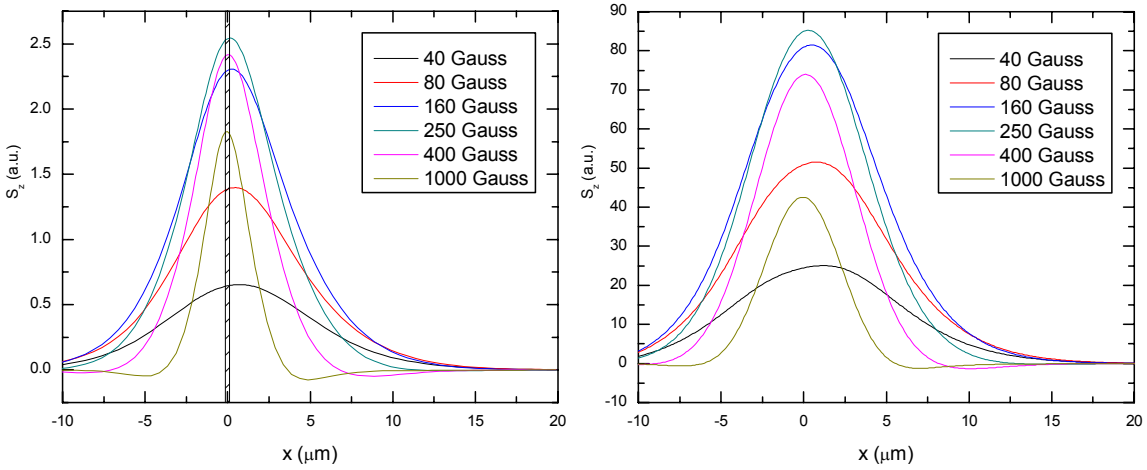

Figure 7.3: Out-of-plane spin concentration (left) and convolution with a Gaussian laser spot with width $w = 2.5$ μm (right) near electrical spin injection electrode for several magnetic fields. The electrode is located at $|x| \leq 0.125$ μm, as indicated by the shaded area on the left.

As can be concluded from these simulations, a maximum out-of plane component arises when a magnetic field of 250 Gauss is chosen, although a field of 160 Gauss will suffice when scanning with a laser spot over the sample. Note that the while spin drift can be recognised in the slightly asymmetrical shape of the profiles, diffusion is the major transport force here.

7.3 Measurements

With the measurement technique described above an attempt is made to optically detect electrically injected spin. First, to locate the ferromagnetic electrodes and to get an indication of the resolution of the optical components in the setup, an x-y scan is made of the reflectivity of the sample (see figure **7.4**) at a probing wavelength of 820 ± 8 nm. At this wavelength, the sensitivity to spin polarisation should be maximal. The electrodes can vaguely be distinguished as the dark blue area between the top

and bottom contact pad. In the microscopic picture the current direction and the *x*-*y* scanning area are indicated. The function generator is connected to the top electrode and the right ohmic contact.

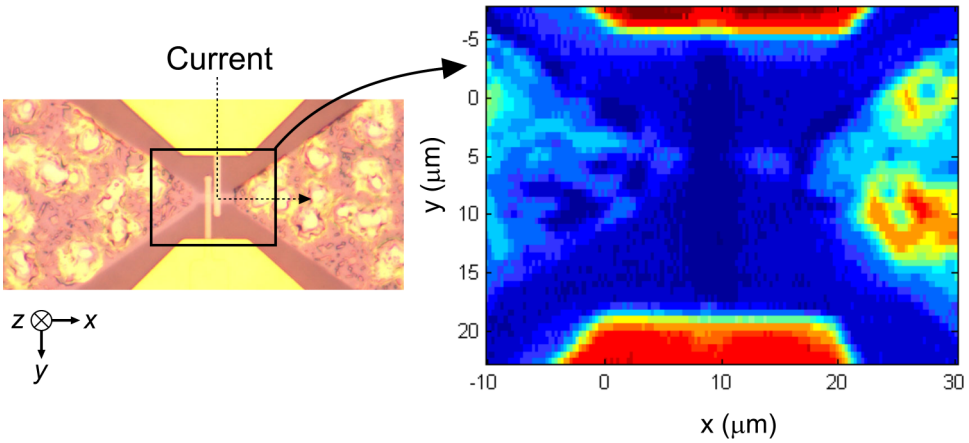

Figure 7.4: Microscopic picture of the all-electrical spin injection and detection device with current direction indicated (left) and reflection from a 820 nm probe spot (right).

For magnetic fields in the *x*-direction ranging from 0 to 380 Gauss, the signal from the two lock-in amplifiers is measured while scanning over the spin transport channel. No out-of-plane spin has been detected though. A possible explanation for this result is that the available signal is estimated to be very weak compared to optically injected spin in the measurements of the previous chapters. For the results published by Crooker, a device with a spin lifetime of 125 ns is used, several orders of magnitude larger than the samples from IMEC. Another difference with our device is the spin diffusion constant, reported to be 10 cm^2s^{-1} for Crooker's device. As a comparison, the simulations for our device are run again, but now with the reported spin lifetime and spin diffusion constant. The other parameters are not changed. The results are shown in figure **7.5**. Note that the same units are used along the *y*-axis as for the left graph in figure **7.3**.

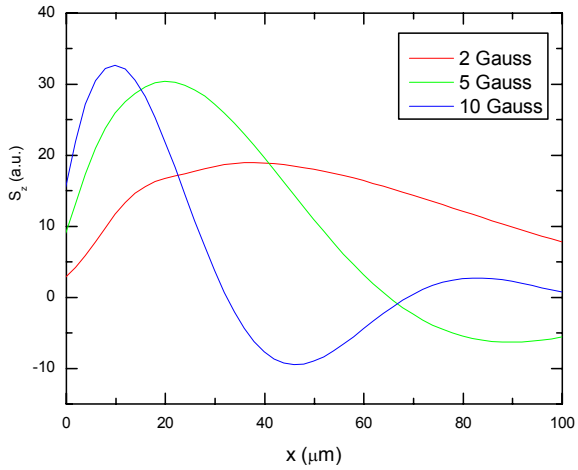

Figure 7.5: Out-of-plane spin concentration near electrical spin injection electrode for several magnetic fields. The electrode is located at $|x| \leq 0.125$ μm, as indicated by the shaded area on the left.

The difference in the maximum between figure **7.5** and figure **7.3** (left) is significant. It indicates that to be able to retrieve any signal from the IMEC device, some parameters could need change. Possibly, improving the sensitivity of the setup suffices though. For example, the laser used for these measurements is not required to pulse. With a continuous laser, there is more time for photon absorption. Per photon, the Kerr effect well could be larger. Anyway, improving the spin lifetime and/or reducing the spin diffusion constant certainly improves the probability that spin is detected optically when it is successfully injected electrically.

7.4 Conclusions

An experimental setup is reported for optical detection of electrically injected spin. Calculations show that the expected signal is significantly smaller in comparison with a successful result on a similar device in literature. This difference is caused by a small spin lifetime and a relatively large spin diffusion constant. At last, the principle of electrical injection of spin polarised electrons has not been proven optically for the IMEC all-electrical spin injection and detection device. A longer spin relaxation time can improve the signal, but the sensitivity of the setup could be improved as well.

8 Conclusions and discussion

In this thesis, the focus has been on exploiting and developing optical techniques to retrieve spin specific parameters from a semiconductor sample. Therefore, optical experiments have been performed, some in the presence of an electric and/or magnetic field. Numerical simulations have been developed to support the experimental work. The sample that was subject to investigation is the design from IMEC Leuven for an all-electrical spin injection and detection device. While its purpose is to show MR, it has proven to be an interesting non-trivial device when investigating it optically.

8.1 The all-electrical spin injection and detection device

The device designed by IMEC Leuven consists of a base semiconductor heterostructure on which insulator/ferromagnetic tunnel junctions are grown laterally. The tunnel barriers can be used to electrically inject and detect spin polarised electrons in the top layer of the semiconductor. Under influence of a magnetic field in the direction of the easy axis of the electrodes, the purpose of the device is to show magnetoresistance, i.e. a change in resistance at the moment one of the ferromagnetic electrodes switches its magnetisation. While this has not been measured yet, the top layer (spin transport layer), consisting of *n*-doped GaAs has proven to be an interesting subject for investigation.

Carrier distribution

Inside the 200 nm thick spin transport layer, the carriers are distributed inhomogeneously as a function of depth. The etching of the surface of this layer causes the band diagram to be not well-defined. This complicates the physics inside the spin transport layer. Because it is an elementary part of the all-electrical spin injection and detection device, determining some properties of this layer can be helpful.

Spin relaxation time

Using Time-resolved Magnetization Modulation Spectroscopy (TiMMS), the electron spin relaxation time of the spin transport layer has been determined to be between 500 ps and 3 ns at a temperature of 5 K. This is in sharp contrast with literature values of bulk *n*-GaAs with the same doping density of $5 \cdot 10^{16}$ cm^{-3}, showing spin relaxation times of up to 125 ns. The inhomogeneous carrier distribution could be responsible for this. Using a magnetic field, the gyromagnetic ratio of the electrons in the sample has been determined to have a value of $6.7 \cdot 10^{9}$ $T^{-1}s^{-1}$.

Spin diffusion and spin mobility

Using TiMMS with a spatially separated spin injection and spin detection laser beam, the spin diffusion and spin mobility constants have been determined. The spin diffusion constant is 45 ± 10 cm^2s^{-1} and the spin mobility is $(1.1 \pm 0.3)\cdot 10^3$ $cm^2V^{-1}s^{-1}$. These values are slightly smaller than values reported in literature for the electrons of *n*-doped GaAs.

Electrical injection

The principle of spin polarised tunnelling from a ferromagnetic layer through an insulator into a semiconductor has already been proven in other devices. When attempting to visualise a spin polarised current through a tunnel junction into the spin transport layer of the IMEC design, no spin polarisation has been detected. The tunnel junctions could thus not be proven to work. The chance to detect electrical spin injection optically would be increased by a longer spin relaxation time or a better sensitivity of the setup used for this measurement.

8.2 Magneto-optical methods for investigating spin properties

During the investigation of the device described above by optical means, some general applicable theories have been set up which could well help in the investigation of spin related parameters in other samples. The magneto-optic Kerr effect has been used as the main source of information in these theories. The Kerr effect is a change in rotational polarisation of a linearly polarised probe laser beam when it is reflected at a spin polarised sample.

Inhomogeneous spin polarised samples

The magneto-optic Kerr effect is phenomenologically defined by the magneto-optical constant Q, being a function of the spin polarisation as well as the wavelength with which a sample is probed. When the spin polarisation in a sample is not homogeneous, the magneto-optic Kerr effect can be defined by the integral of the relational function $f_\lambda(z)$ with the z-dependent Q. This relational function can be calculated numerically for a known (estimation of) $Q(z)$, but could possibly also be used to reconstruct $Q(z)$ when the magneto-optic Kerr effect is measured. For the spin transport channel probed with different wavelengths, a correspondence could been shown between measurements and a calculation using $f_\lambda(z)$ defined for the heterostructure.

Spin diffusion and asymmetrical recombination

While measuring spin diffusion of an optically injected Gaussian spin package in a semiconductor, it is hard to distinguish between true spin diffusion and non-linear asymmetrical spin recombination, both causing the spin package to broaden. Once electrons and holes are recombined, spin diffusion can be determined more reliably.

9 Literature

[1] Gordon E. Moore, *Cramming more components onto integrated circuits*, Electronics **38**, 8 (1965)

[2] M.N. Baibich, J.M. Broto, A. Fert, F. Nguyen Van Dau, F. Petroff, P. Eitenne, G. Creuzet, A. Friederich and J. Chazelas, *Giant Magnetoresistance of (001)Fe/(001)Cr Magnetic Superlattices*, Phys. Rev. Lett. **61**, 2472 - 2475 (1988)

[3] P.H. Song and K.W. Kim, *Spin relaxation of conduction electrons in bulk III-V semiconductors*, Phys. Rev. B **66**, 035297 (2002)

[4] I. Žutić and J. Fabian, *Silicon twists*, Nature **447**, 269 (2007)

[5] S. Datta and B. Das, *Electronic analog of the electro-optic modulator*, Appl. Phys. Lett. **56**, 665-667 (1990)

[6] P. van Dorpe, R. Vanheertum, H. Boukari, W. van Roy and G. Borghs, *Design of the tunnel contacts and the transport region of all-electrical spin-injection-detection devices*, J. Appl. Phys. **99,** 08S702 (2007)

[7] J.J.H.M. Schoonus, O. Kurnosikov, H.J.M. Swagten, B. Koopmans, E.J. Geluk, F. Karouta, W. van Roy and G. Borghs, *Towards all-electrical spin injection and detection in GaAs*, Phys. Stat. Sol. (c) **3,** 4176-4179 (2006)

[8] D.J. Hilton and C.L. Tang, *Optical Orientation and Femtosecond Relaxation of Spin-Polarized Holes in GaAs*, Phys. Rev. Lett. **89**, 146601 (2002)

[9] J.R. Chelikowsky and M.L. Cohen, *Nonlocal pseudopotential calculations for the electronic structure of eleven diamond and zinc-blende semiconductors*, Phys. Rev. B **14**, 556-582 (1976)

[10] C. Kittel, *Introduction to solid state physics*, John Wiley & Sons, Inc., New York, (1996)

[11] S. Adachi, *Properties of group-IV, III-V and II-VI semiconductors*, Wiley, Chichester (2005)

[12] R.I. Dzhioev, K.V. Kavokin, V.L. Korenev, M.V. Lazarev, B.Ya. Meltser, M.N. Stepanova, B.P. Zakharchenya, D. Gammon, and D.S. Katzer, *Low-temperature spin relaxation in n-type GaAs*, Phys. Rev. B **66**, 245204 (2002)

[13] Z.G. Yu and M.E. Flatté, *Spin diffusion and injection in semiconductor structures: Electric field effects*, Phys. Rev. B **66**, 235302 (2002)

[14] M.E. Flatté and J.M. Byers, *Spin Diffusion in Semiconductors*, Phys. Rev. Lett. **84**, 4220 (2000)

[15] H.J.M. Swagten, *Magnetism and Magnetic Materials*, Course syllabus (2006)

[16] K.H. Bennemann, *Non-linear optics in metals*, Oxford University Press, Oxford (1998)

[17] J. Zak, E.R. Moog, C. Liu and S.D. Bader, *Magneto-optics of multilayers with arbitrary magnetization directions*, Phys. Rev. B **43**, 6423 (1991)

[18] P.R. LeClair, *Fundamental aspects of spin polarized tunneling*, PhD thesis, Eindhoven University of Technology (2002)

[19] V.F. Motsnyi, P. van Dorpe, W. van Roy, E. Goovaerts, V.I. Safarov, G. Borghs and J. de Boeck, *Optical investigation of electrical spin injection into semiconductors*, Phys. Rev. B **68**, 245319 (2003)

[20] S.A. Crooker, M. Furis, X. Lou, C. Adelmann, D.L. Smith, C.J. Palmstrøm, P.A. Crowell, *Imaging Spin Transport in Lateral Ferromagnet/Semiconductor Structures*, Science **309**, 2191 (2005)

[21] M. van Kampen, *Ultrafast spin dynamics in ferromagnetic metals*, PhD Thesis, Eindhoven University of Technology (2003)

[22] D.W. Jenkins, *Optical constants of $Al_xGa_{1-x}As$*, J. Appl. Phys. **68**, 1848-1853 (1990)

[23] M.D. Sturge, *Optical Absorption of Gallium Arsenide between 0.6 and 2.75 eV*, Phys. Rev. **127**, 768-773 (1962)